Volume 54
Number 31
21 August 2025
Pages 11759-12052

Dalton Transactions

An international journal of inorganic chemistry

rsc.li/dalton

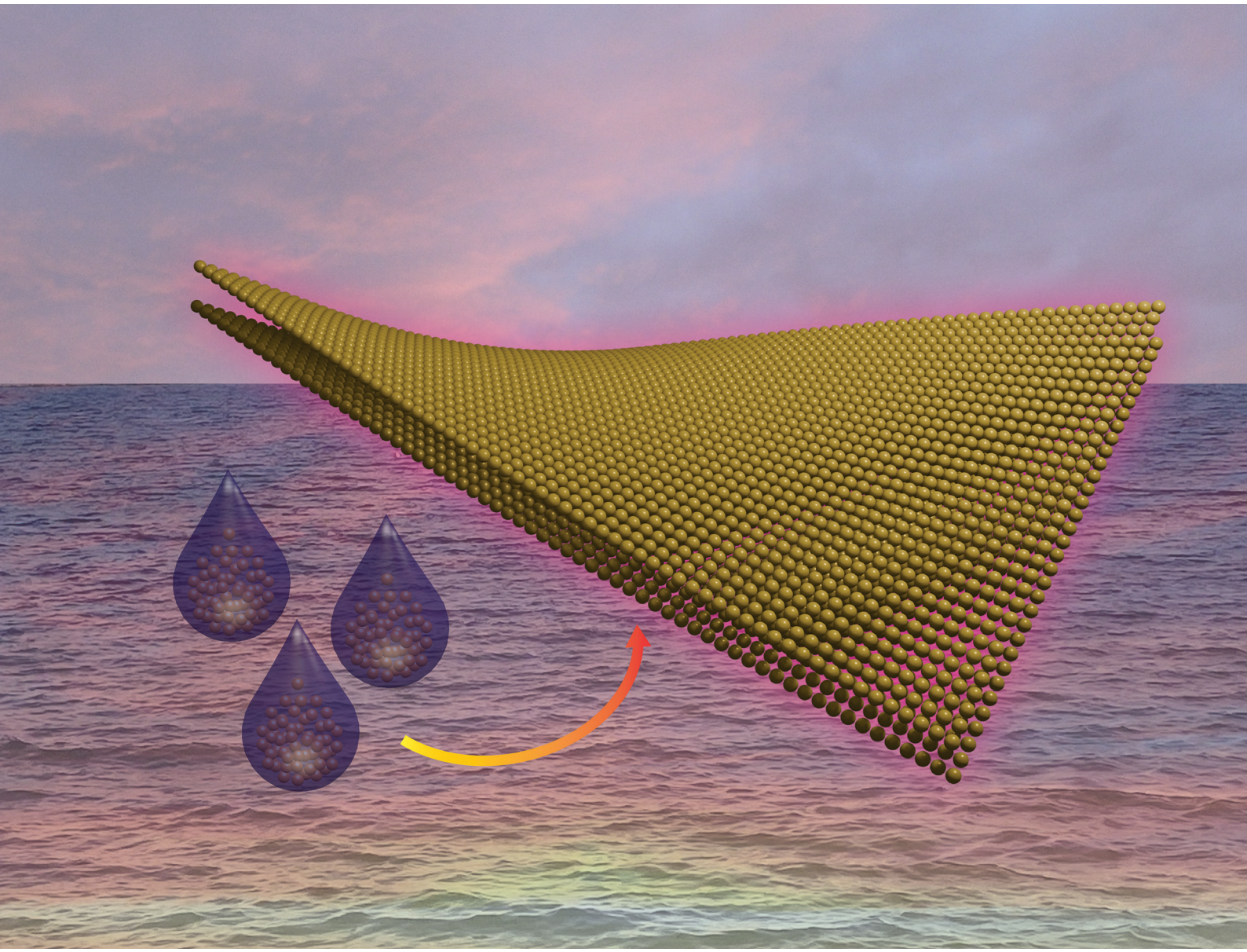

ISSN 1477-9226

ROYAL SOCIETY OF CHEMISTRY

PERSPECTIVE

Venishaa Sethumadhavan and Nonappa

Atomically precise noble metal nanoclusters for engineering self-assembled two-dimensional materials

Dalton Transactions

ROYAL SOCIETY OF CHEMISTRY

PERSPECTIVE

View Article Online
View Journal | View Issue

Cite this: *Dalton Trans.*, 2025, **54**, 11770

Atomically precise noble metal nanoclusters for engineering self-assembled two-dimensional materials

Venishaa Sethumadhavan and Nonappa *

Two-dimensional nanomaterials derived from noble metals exhibit unique optoelectronic properties with potential applications in advanced nanodevices, catalysis, imaging, biomedicine, and sensing. Over the years, atomically precise noble metal nanoclusters have emerged as promising building blocks for self-assembled discrete and hierarchical colloidal superstructures. Various approaches, including templated growth, air–water interfaces, and non-covalent interactions between surface ligand functional groups, have been utilized to promote the self-assembly of nanoclusters. However, until recently, the self-assembly of nanoclusters into ultrathin, free-standing, two-dimensional materials across length scales has remained challenging. In this perspective article, approaches for the fabrication of self-assembled gold and silver nanocluster-based films, 2D nanosheets, colloidal crystals and macroscopic membranes are discussed. We present the self-assembly principles and insights into how such assemblies enable altered optoelectronic properties, mechanical performance, catalytic activities, enhanced sensing, and device performance. Finally, we highlight how nanocluster-based two-dimensional assemblies offer the emergence of new optoelectronic properties, still retaining the intrinsic properties of individual building blocks.

Received 18th May 2025,
Accepted 4th July 2025

DOI: 10.1039/d5dt01171j

rsc.li/dalton

Introduction

Ultrathin two-dimensional (2D) nanomaterials display high specific surface area, exceptional mechanical performance and optoelectronic properties.[1] The demonstration of mechanical exfoliation of atomically thin graphene layers has triggered a revolution in the discovery and characterization of a wide range of 2D nanomaterials.[2] Graphene is a lightweight and flexible material with high mechanical strength, optical transparency and intrinsic carrier mobility, making it a versatile material in electronics,[3] photonics,[4] energy storage,[5] and thermal management applications.[6] 2D nanomaterials, including hexagonal boron nitride (hBN),[7] transition metal dichalco-

Faculty of Engineering and Natural Sciences, Tampere University, FI-33720 Tampere, Finland. E-mail: nonappa@tuni.fi

Venishaa Sethumadhavan

Venishaa Sethumadhavan is a Doctoral Researcher at the Faculty of Engineering and Natural Sciences, Tampere University, Finland. She holds a Bachelor of Science in Microbiology with Nanotechnology from Nehru Arts and Science College, Coimbatore, India, and a Master of Science in Nanoscience and Technology from Bharathiar University, India. Her research focuses on nanomaterials and the development of nanoparticle-based probes for advanced bioimaging applications.

Nonappa

Nonappa is an Associate Professor at the Faculty of Engineering and Natural Sciences at Tampere University, Finland. He received his Ph.D. (2008) from the Indian Institute of Science, Bangalore, India. He conducted his postdoctoral research at the University of Jyväskylä and Aalto University, Finland. His research interests include precision nanomaterials, colloids, hydrogels, bio-based optical fibers, in vitro cancer models, cryogenic transmission electron microscopy, and electron tomography.

genides (TMDs),[8] layered double hydroxides,[9] graphitic carbon nitrides,[10] silicene,[11] and MXenes,[12] 2D polymers,[13] metal organic frameworks (MOFs),[14] covalent organic frameworks (COFs),[15] and metallic 2D nanomaterials,[16] have been have been studied extensively for applications in flexible electronics/optoelectronics,[17] catalysis,[18] energy storage,[19] and wearable sensors.[20] The synthesis, characterization, and application of these 2D materials have been extensively reviewed in the literature and are beyond the scope of this review.[21] In brief, 2D nanomaterials have been prepared using either top-down or bottom-up synthetic strategies. The top-down approach utilizes either mechanical or liquid-phase exfoliation from the bulk three-dimensional (3D) layered materials to obtain atomically thin 2D layers. The success of mechanical exfoliation is attributed to the weak interlayer van der Waals interactions compared to the strong intralayer bonding. These weak interlayer interactions can be readily overcome by external mechanical forces, such as those provided by an adhesive tape, to achieve high-quality 2D layers. However, mechanical exfoliation suffers from low yield, limited size of the 2D layers and contamination from residual adhesives.[21] A recent approach involves depositing a thin film of gold onto a substrate, followed by pressing 3D bulk crystals against the gold substrate and adhesive tape-assisted mechanical exfoliation to obtain large-scale monolayers.[22] While this approach produces millimetre-scale monolayers with high yield, it requires post-cleaning to remove the metal layer and is substrate-dependent. Exfoliation can also be performed in the liquid phase using ultrasonication or shear mixing to overcome the inter-layer interactions of layered materials in an appropriate solvent.[23,24] In the liquid phase either direct or surfactant-assisted exfoliation is used. Surfactants can intercalate between the layers, weakening the interlayer bonds and facilitating exfoliation. Liquid-phase exfoliation is a scalable and cost-effective process. However, the process utilizes toxic solvents, and ultrasonication results in structural damage, leading to nanosheets with smaller lateral dimensions. Furthermore, limited control over intercalation depth results in incomplete exfoliation or structural defects.[25]

The bottom-up approaches to preparing 2D nanomaterials include chemical vapor deposition (CVD),[26] physical vapor deposition (PVD),[27] molecular beam epitaxy (MBE),[28] and atomic layer deposition (ALD).[29] In CVD and PVD, gaseous or solid precursors are used and involve thermal decomposition, chemical synthesis, and chemical transport reactions to obtain the desired products. By controlling the flow rate of the precursors, the morphology, size and structure can be accurately controlled.[26,27] Molecular beam epitaxy (MBE) produces high-quality films on crystalline substrates under ultra-high vacuum with sub-nanometre precision.[28] MBE is suitable for materials with high thermal stability; however, it is cost-intensive and has a slow growth rate, which presents a hurdle for the large-scale production of 2D materials. Atomic layer deposition enables the fabrication of thin films layer by layer on a substrate through sequential, self-limiting surface reactions between gaseous precursors, allowing for sub-nanometre precision.[29] ALD can be performed at relatively low temperatures, but it suffers from a low deposition rate, the need for expensive equipment, and is limited to certain precursors. Solid state photopolymerization of monomer crystals has been utilized to obtain 2D polymers, that were readily exfoliated into nanoporous monolayer sheets.[13] However, such methods require predefined monomers with specific functionalities and are not generic. Metal organic frameworks (MOFs) and covalent organic frameworks (COFs)-based monolayer and multilayered 2D nanostructures have been prepared on substrates.[14,15] Because of their modular structures, high surface areas, and dimension-dependent optoelectronic properties, they find applications in energy storage, catalysis, gas separation, sensing and thermoelectric materials.[30–34] Despite their promising properties, they face challenges in scalability, control over layer thickness, mechanical and chemical stability and processability.

Recently, considerable attention has been directed towards noble metal-derived metallic 2D nanomaterials.[16] They offer potential applications, including catalysis, sensing, bioimaging, nanodevices, solar cells and therapeutics. However, for metals, the highly symmetric crystal lattice promotes 3D crystal growth, rendering 2D morphology thermodynamically unfavoured. In the literature, top-down and bottom-up approaches have been demonstrated for the synthesis of noble metal-derived 2D nanomaterials.[35] The top-down approach utilizes mechanical compression, exfoliation and nanolithography to achieve ultrathin nanosheets. The mechanical compression exploits the ductile nature of noble metals to achieve nanolayers. For example, Liu *et al.* have demonstrated that repeated folding and calendaring of metal foils (Au, Ag, Cu, Fe, and Al) results in size reduction and yields 2D metallic nanosheets.[36] In another approach, Huang *et al.* used platinum (Pt) sputtering on a silicon substrate, followed by heat pressing to obtain nanosheets with a thickness of 5 nm.[37] Funatsu *et al.* reported the liquid phase exfoliation of layered Pt precursors in the presence of sodium dodecyl sulfate (SDS).[38] Nanolithography techniques, including electron beam lithography and focused ion beam milling, allow the construction of 2D arrays on substrates.[39]

Metals are non-layered structures, limiting the application of methods such as mechanical exfoliation, which is typically utilized for van der Waals layered materials. Therefore, the synthesis of metallic 2D nanomaterials is primarily achieved using bottom-up strategies under solution-phase colloidal synthesis, which requires symmetry breaking and anisotropic growth through kinetic control during the growth pathway.[40] Kinetic control can be achieved by either slowing down the atom addition process or lowering the total free energy of the nanostructures.[41] Due to the high surface-to-volume ratio in 2D metallic nanomaterials, the surface energy is the main contributor to the total free energy. The surface energy of nanostructures can be reduced by using organic ligands, polymers, or biomolecules as capping agents, enhancing their stability. In the bottom-up approach, metallic 2D nanomaterials have been synthesized using ligand-assisted synthesis, templated

synthesis, seeded growth, solvothermal synthesis, phase transition, and nanoparticle self-assembly.[16] The ligand-assisted synthesis utilizes the functional groups and the affinity of organic ligands to certain metals.[42] Here, the interaction between the ligands and metal atoms plays a critical role in directing the 2D nanostructure formation. First, ligand adsorption reduces the surface energy of specific metal facets, thereby stabilizing the system by minimizing the total free energy. Secondly, certain metal–ligand complexes tend to arrange themselves into 2D layers, acting as self-templating for 2D morphologies. Third, long-chain organic ligands offer strong steric hindrance, which prevents aggregation and promotes the formation of flat 2D structures. The type, charge and functional groups of ligands have been shown to affect the final morphology of 2D nanostructures.[43] A variety of nanostructures, including circular dendritic nanosheets,[44] nanodisks,[45] nanoplates,[46] and nanobelts,[47] have been successfully synthesized using ionic, non-ionic and polymer ligands as well as small molecules such as CO, halides, and metal cations. Anisotropic growth of 2D nanostructures can also be achieved by confining nucleation and directing morphology using physical or chemical templates.[48] 2D substrates such as graphene, graphene oxide, TMDs, and layered hydroxides have been used to achieve ultrathin nanosheets and crystal phase heterostructures. *In situ* reduction within interlayer spaces or at self-assembled interfaces has been shown to produce ultrathin, single-crystalline nanosheets with tunable thickness and lateral dimensions.[49] Seeded growth is one of the versatile bottom-up strategies for synthesizing well-defined mono-, and multimetallic 2D nanostructures.[50] By using high-quality seeds and selective ligand-mediated facet growth, seeded growth offers tunable shapes and dimensions such as ultrathin Ag nanoplates and nanosheets.[51]

Despite tremendous progress in preparing various metallic 2D nanostructures, achieving large-scale, macroscopic structures using the above approaches remains a major challenge in modern nanotechnology. In this context, the self-assembly of noble metal nanoparticles (NPs) has emerged as an attrac-

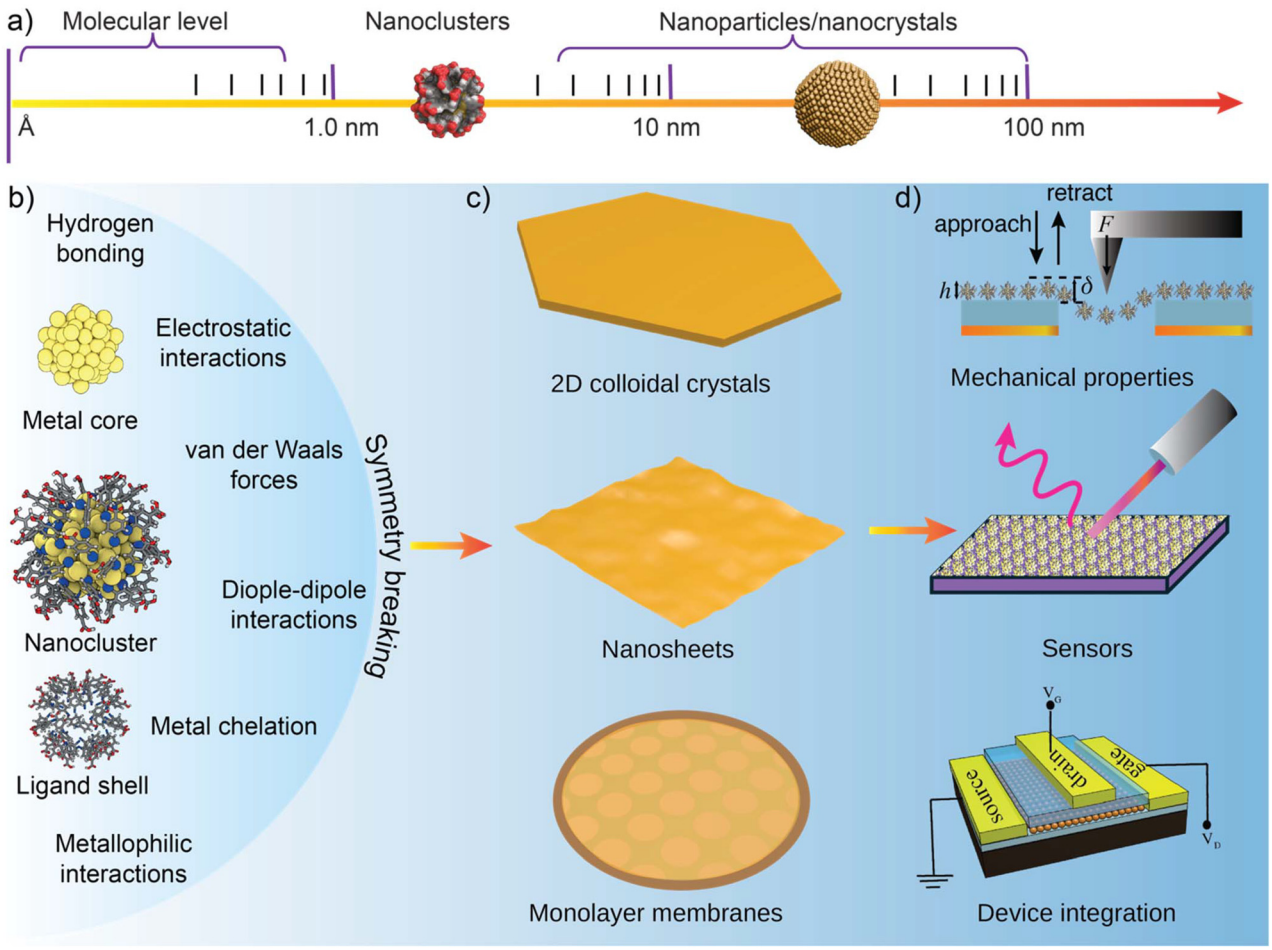

Fig. 1 An overview of the contents discussed in this review. (a) Atomically precise nanoclusters are a bridging link between large plasmonic nanoparticles and small molecules. (b) Atomically precise nanoclusters with exactly defined molecular structure promote self-assembly *via* various non-covalent interactions. (c) Schematic illustration of 2D assemblies such as colloidal crystals, nanosheets and monolayer membranes. (d) The self-assembled structures exhibit unique optoelectronic and mechanical properties, with potential applications as substrates for enhanced sensing and device fabrication.

tive method for constructing metallic 2D nanostructures.[52] Noble metal nanoparticles with diverse sizes, shapes, compositions, and tunable optoelectronic properties are ideal colloidal building blocks for achieving multifunctional 2D nanomaterials across various length scales.[53] In this review, we will introduce the challenges in preparing 2D nanomaterials using metal nanoparticle self-assembly and the need for atomically precise nanoparticle building units for fabricating precision 2D nanomaterials across the length scale with reproducible optical properties, mechanical performance and sensing capabilities. We will highlight recent progress in using atomically precise noble metal nanoclusters (NCs) as building blocks for 2D nanomaterials across various length scales. Specifically, we will focus on approaches to generate (i) substrate-assisted assembly, (ii) 2D nanosheets and colloidal crystals, and (iii) free-standing 2D monolayers. We will highlight emerging properties, such as mechanical behavior, optoelectronic properties, device integration, and sensing applications (Fig. 1).

Noble metal nanoparticle self-assembly

Due to their high surface-to-volume ratio, noble metal nanoparticles exhibit high surface energy.[54] As a result, the nanoparticles undergo uncontrolled aggregation, thereby reducing the surface energy. Due to their tendency for uncontrolled aggregation, polydispersity, non-uniform ligand density, and batch-to-batch variation, the self-assembly of large plasmonic nanoparticles results in inconsistent structures and properties.[55] Furthermore, the lack of directional interactions and slow diffusion at the colloidal scale can lead to structural heterogeneity and non-uniform aggregates.[56] Various inter-nanoparticle forces such as van der Waals forces, electrostatic, and steric interactions, have been shown to play a central role in nanoparticle self-assembly. However, the exact role of these interactions and their dependence on the nanoparticle size, shape and surface chemistry is not completely understood.[57] Furthermore, the understanding of the effect of solvent and other environmental parameters is not fully matured.[58] More importantly, template-free assembly of 1D or 2D layered structures is a major challenge as the high surface energy of the nanoparticles tends to destabilize such structures.[59] Moreover, the inherent isotropic nature, of the spherical nanoparticles drives 3D assemblies instead of anisotropic 1D or 2D structures. Therefore, symmetry breaking and anisotropic interactions between nanoparticles must be introduced to obtain 2D structures. The inhomogeneous surface charge in plasmonic nanoparticles can induce electrical dipoles. This will enable dipole–dipole interactions strong enough to overcome thermal fluctuations and coulombic repulsions to obtain 1D assemblies.[60] Anisotropy can also be achieved using external magnetic and electrical fields, selective ligand exchange, DNA functionalization, and spatial and shear confinement to achieve controlled 1D and 2D assemblies of nanoparticles.[61] Nanoparticle self-assemblies are driven by inter-nanoparticle interactions mediated by the capping organic ligand molecules.[62] Therefore, the ligand type, functional group, charge, and density play a critical role in promoting the self-assembly and controlling the dimensional characteristics of resulting structures. Computational simulations, including molecular dynamics (MD), coarse-grained (CG), and Monte Carlo (MC) simulations, have been employed to understand the effects of ligand density and intermolecular forces at the nanoscale on nanoparticle self-assembly.[63] MD simulation of dodecanethiol-capped AuNP self-assembly revealed that van der Waals interactions between the ligands are dominated when self-assembly was performed at the toluene-water/ethanol interface. More importantly, the self-assembly is also influenced by the evaporation rate, as 2D assemblies were obtained through slow solvent evaporation.[63] Ligand functional groups also influence the self-assemblies. For example, fast and random aggregation was observed when dodecanethiol was replaced with mercaptoundecanoic acid. This is attributed to strong hydrogen bonding and the polarization effect of mercaptoundecanoic acid. Furthermore, the self-assembly was found to be independent of the evaporation rate. The nanoparticle size, aspect ratio, shape anisotropy, and surface energy have been shown to affect the final self-assembled structures. For example, it has been shown that under electric field directed assembly, larger nanoparticles (d ~20–40 nm) formed uniform monolayer due to stronger dipolar interactions and polarizability.[64] Whereas the smaller nanoparticles (d ~5–15 nm) lead to smaller clusters and defects due to weaker interactions. Furthermore, lower surface energy in larger nanoparticles have been shown to promote uniform assemblies.[65] By tuning these parameters, 2D close-packed arrays of AuNPs, binary superlattices, and nanoparticle–polymer composite arrays have been successfully fabricated using evaporation-induced assembly, electrostatic assembly, interfacial assembly, binary solvent approaches, antisolvent techniques, dip coating, and Langmuir–Blodgett film formation.[66] These strategies are promising, given that self-assembled 2D materials composed of plasmonic gold (Au) NPs and silver (Ag) NPs exhibit unique mechanical properties, enhanced sensing, and improved device performance.[67,68]

Mueggenburg *et al.* have studied the evaporation-induced assembly of dodecane thiol ligand-capped gold NPs (9.4 nm) to achieve monolayer membranes. The membranes exhibited a highly scattered elastic modulus, ranging from 3 to 39 GPa.[67] The study suggests that the batch-to-batch variation in nanoparticles leads to uncertainty and compositional differences in membranes. Deoxyribonucleic acid ligands offer complementary hydrogen bonding and tunable inter-nanoparticle distance for nanoparticle assemblies. Cheng *et al.* used DNA-capped nanoparticles with tunable inter-nanoparticle distances to fabricate membranes using a microhole drying method, resulting in Young's moduli within a narrow range of 6.49 ± 1.57 GPa.[69] However, the observed average moduli values are much less than those of other NP membranes. This is attributed to the non-specific interactions of DNA bases of neighbouring nanoparticles. In ligand-protected metal NP-

based assemblies, the core-core interactions account for less than 10% of the overall strength of the self-assembled material, suggesting the significance of surface ligands.[70] However, achieving reproducible nanostructures using plasmonic NP is still a major challenge. The size and composition uniformity of the building blocks are key determining factors in the formation of uniform structures, optoelectronic properties, and reproducible mechanical performance of self-assembled materials. More importantly, it has been hypothesized that in NP-based 2D structures, the mechanical property depends on ligand interdigitation and packing efficiency of NPs. Therefore, surface ligands are crucial in stabilizing the NP self-assembled structures. Preparing uniform structures with reproducible structure and optomechanical properties is crucial for the fabrication of advanced nanodevices, where nanoparticle size and ligand density play a significant role. Therefore, identifying building blocks with uniform size, composition, ligand density and methods for fabricating 2D nanomaterials is one of the most important challenges in modern nanotechnology, which forms the basis of precision and functionality for real-world applications.[71]

Atomically precise noble metal nanoclusters

Atomically precise gold (Au) and silver (Ag) nanoclusters (NCs) are attractive nanoscale units because of their unique optoelectronic properties, with readily tunable structure, size, shape, composition and surface ligand functional groups.[72] With a history of more than six decades, the fundamental understanding of the structure, composition and optoelectronic properties of NCs has been significantly refined.[73] The combination of advanced characterization and analytical techniques such as mass spectrometry, single crystal X-ray diffraction, small angle X-ray scattering, small angle neutron scattering, electron microscopy, and computational simulations has shaped the understanding of the structure and origin of their unique optoelectronic properties.[74] New insights on the importance of size, metal atom composition and ligand chemical structure in modulating the physicochemical properties of NCs and their stability are in a state of rapid development. First-principles-based computational modeling has also been employed to probe the structural and electronic properties of nanoclusters. Notably, the 'divide-and-protect' and 'superatom' theories have been proposed to explain the structural characteristics of AuNCs and magic-number NC stability, respectively.[75] The molecular structure of NCs allows reaction between clusters, selective doping, and controlled ligand exchange with high specificity and accuracy.[76–78] Several research groups have extensively reviewed the synthesis, characterization, optoelectronic properties and structure–property relationships of NCs.[79–81] Because of their atomically precise structure with an exact number of metal atoms and covalently linked ligands, NCs have emerged as excellent candidates for self-assembled multifunctional materials through precision nanoengineering.[53] The ligand shells offer improved stability and prevent the coalescence or random aggregation of NCs. Furthermore, the inter-NC interaction mediated by the ligand functional groups offers routes for a highly ordered arrangement of NCs. Notably, the inter-NC interactions and distances can be readily tuned by modifying the functionalities of ligands. Therefore, the limitations observed in plasmonic NPs, such as batch-to-batch variation and uncertainty in size and ligand density, can be addressed through the use of NCs. It is well established that in their solid state, the inter-NC interactions are mainly driven by surface ligands through non-covalent interactions, including hydrogen bonding, electrostatic, dipolar, π-stacking, metal coordination, and van der Waals interactions.[81] It has been demonstrated that cluster-assembled crystals show unique photoluminescence and mechanical properties in their solid state.[82] Their molecular structure allows a wide range of cluster-assembled materials, including co-crystals,[83,84] polymorphs,[85] hybrid materials,[86] and bimetallic structures.[87] Due to its supramolecular nature, these interactions can be readily manipulated using a range of stimuli such as solvent polarity, pH, temperature, light irradiation, and metal coordination. Therefore, structures other than 3D crystals can be obtained, provided appropriate methods are identified. Self-assembly of NCs offers routes for multifunctional structures with tunable size, shape, stability, catalytic activity, optical properties and mechanical performance.[53,79–81,88] One of the emerging approaches is to utilize nanoclusters to generate ultrathin two-dimensional (2D) materials.

Two-dimensional assemblies of NCs on substrates

Among AuNCs, triphenylphosphine (PPh_3) ligand-protected $Au_{55}(PPh_3)_{12}Cl_6$ is one of the most extensively studied NCs.[89] The Au_{55} NC has a metal core size of 1.4 nm with a ligand shell thickness of 0.35 nm, resulting in an overall size of the NC~2.1 nm. The early experiments based on current–voltage (*I–U*) studies of individual Au_{55} NCs revealed their potential to act as single-electron transistors (SETs) at room temperature.[90] Therefore, it was hypothesized that highly ordered two-dimensional assemblies of such NCs may allow correlated single electron tunneling (SET) for next-generation nanoelectronics. Peschel and Schmid made one of the early attempts to prepare monolayer assemblies of $Au_{55}\{PPh_2(m\text{-}C_6H_4SO_3H)_{12}\}Cl_6$ on mica substrates (Fig. 2).[91] The immersion of a mica substrate coated with polyethyleneimine (PEI) into an aqueous solution of NC resulted in a monolayer assembly of NCs on the mica substrate (Fig. 2a). The electrostatic interaction between the negatively charged sulfonic acid groups on NCs and positively charged PEI on the mica substrate allows strong adhesion of NCs on the substrate. Atomic force microscopy (AFM) images of the NC assemblies on the mica surface revealed regularly arranged NCs with an inter-NC distance of 2.4 ± 0.2 nm

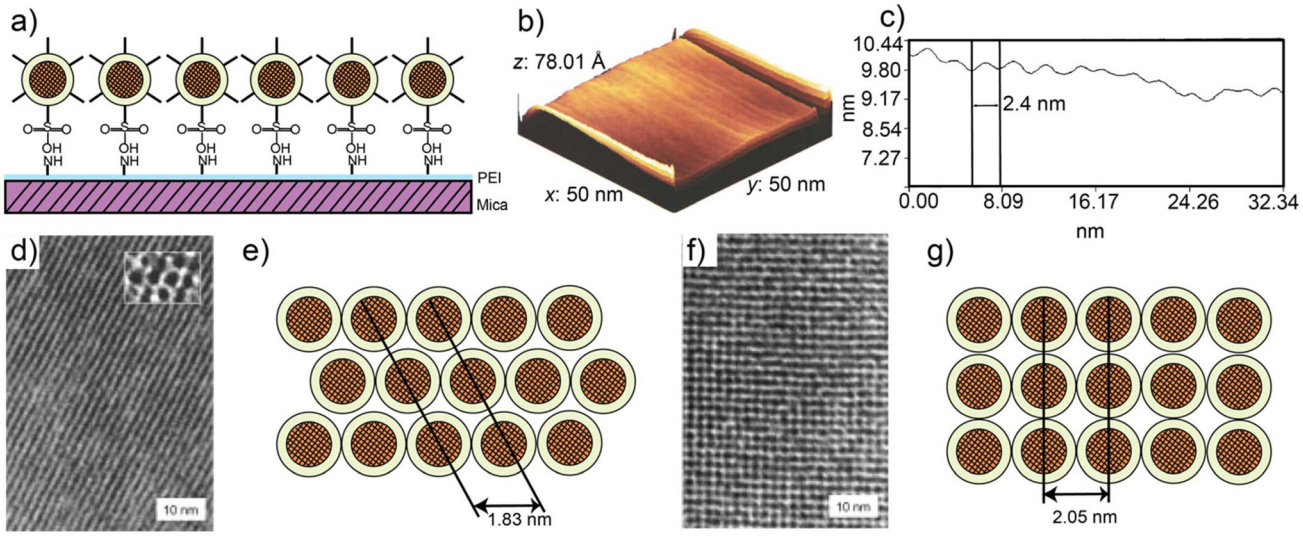

Fig. 2 Self-assembled monolayer arrays of NCs on substrates. (a) Schematic illustration of $Au_{55}\{PPh_2(m\text{-}C_6H_4SO_3H)_{12}\}Cl_6$ NC on PEI-coated mica substrate. (b and c) AFM image of monolayer film and corresponding height profile. Reproduced with permission from ref. 91 Copyright © 1995 Wiley-VCH. (d) TEM image showing a hexagonally close-packed array of $[Au_{55}(Ph_2PC_6H_4SO_3H)_{12}Cl_6]$ NC on carbon substrate. (e) Schematic illustration of hcp arrays of NCs. (f) TEM image showing a cubic close packed array of $[Au_{55}(Ph_2PC_6H_4SO_3H)_{12}Cl_6]$ NC on carbon substrate. (g) Schematic illustration of ccp arrays of NCs. Reproduced with permission from ref. 92 Copyright © 2000 Wiley-VCH.

(Fig. 2b and c). This study suggests that polyelectrolytes, such as cationic PEI with a uniform coating over a substrate, can be utilized for the uniform assembly of monolayers of negatively charged NCs. In another study, Schmid *et al.* reported the fabrication of close-packed 2D arrays of $[Au_{55}(Ph_2PC_6H_4SO_3H)_{12}Cl_6]$ NCs on a carbon substrate.[92] The 2D monolayer assembly was achieved using dip coating-assisted assembly on a TEM grid with a carbon support film. The TEM grid was coated with low molecular weight (60,000 g mol^{-1}) polyethylene imine (PEI) polymer and was immersed in NC solution to obtain a monolayer of clusters through electrostatic assembly. The resulting 2D assembly displayed two types of NC packings, *viz.*, hexagonal close packing and cubic close packing (Fig. 2d–g). The hexagonal form showed the distance between neighboring NC rows of 1.83 nm along the {111} direction (Fig. 2e). On the other hand, the cubic orientation revealed the inter-NC distance of 2.05 nm between adjacent rows (Fig. 2g).

However, the exact reason that drives the formation of both hexagonal and cubic close packing is not known. It may arise from the interplay of thermodynamic, kinetic, and nanoparticle-specific parameters, such as size, shape, and interactions. Furthermore, hcp and ccp structures have nearly identical packing efficiencies and free energies.[93] The minimal energy difference between these structures suggests that a slight variation in assembly conditions can favor one form over the other. Niesen and Rand reported the NC thin films for light emitting diodes (LED) using solution processing of glutathione-capped AuNCs and AgNCs by phase transferring to toluene (Fig. 3a).[94]

The spin casted film furnished a few-layer thick film of 5.3 ± 0.8 nm corresponding to 3–4 layers of NCs. The film was utilized to fabricate light-emitting diodes (LEDs) by sandwiching the AuNC layers between an indium tin oxide (ITO) cathode on a glass substrate with zinc oxide (ZnO) as an electron injecting layer and an organic hole transport layer. The electroluminescent (EL) spectrum of the AuNC LED at 1.74 V displayed an emission band centered at 750 nm, identical to the photoluminescent spectrum measured from the AuNC dispersion in toluene (Fig. 3b and c). This indicates that the emission originates from the AuNCs in the LED device. Similar results were also obtained when Ag NCs were used instead of AuNCs, with an EL band centered at λ = 697 nm from the AgNC device. This work suggests that the NC-based LED devices can be readily tuned by altering the composition of NCs. Qin *et al.* reported the methanol sensing using silver nanoclusters, $\{[Ag_{12}(L)_2(CO_2CF_3)_{14}(H_2O)_4(AgCO_2CF_3)_4](HNEt_3)_2\}_n$ L = 1-(3-mercaptoprop-1-en-2-yl)-2-methoxypyridin-1-ium.[96] The sensor fabrication was performed by casting a film of AgNC in aqueous hydroxypropyl methylcellulose over the PET substrate and attaching copper wires to the thin films. Here, the AgNC-based film acted as an insulator under dry conditions and upon exposure to protic organic solvents such as methanol and ethanol, the film turned conductive. Importantly, when exposed to aprotic solvents, the film remained as an insulator. Furthermore, the electric current turned to zero again with the removal of methanol or ethanol from the thin films, indicating that the protic organic solvents should interact with the AgNCs to make them conductive. The relative capacitance change of the AgNC sensor for methanol can reach up to 5000 for the mixture of 3 : 7 (v/v) methanol : water. The observed change in capacitance was ~33 times higher than that reported in the literature for cellulose/graphene nanocomposites. Ligand and metal composition engineering

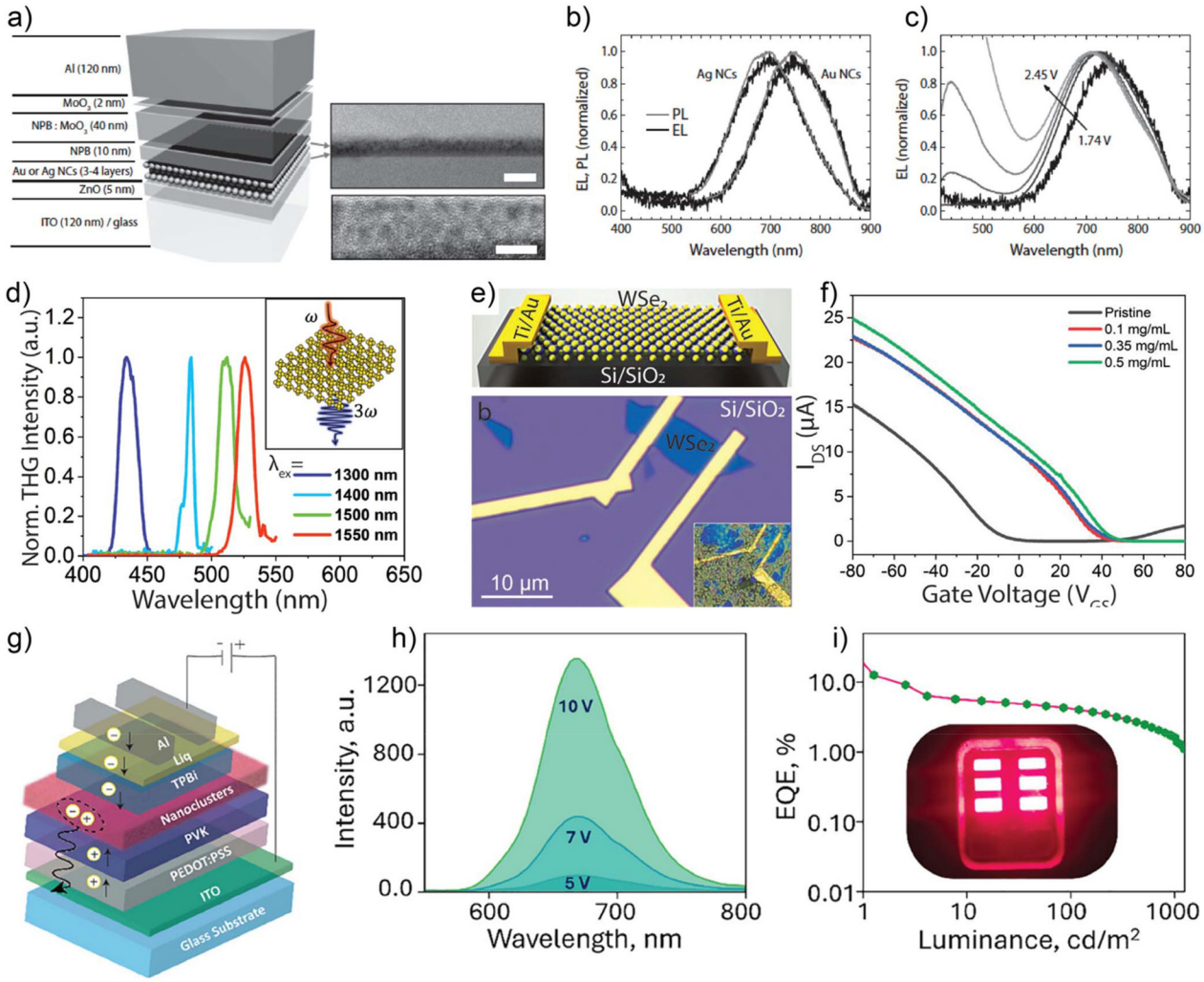

Fig. 3 NC incorporated devices. (a) Schematic illustration of an LED device incorporating AuNCs. (b) TEM image showing the cross-sectional view of the ZnO/Au NC layer (top) and individual NCs in the Au NC layer (bottom). (c) Normalized electroluminescence (EL) and photoluminescence (PL) spectra of NC incorporated LEDs and NCs dispersed in toluene. (c) Voltage dependence of the EL spectra of Au NC-LED at biases between 1.74 V-2.45 V. Reproduced with permission from ref. 94 Copyright © 2014 Wiley-VCH. (d) Third harmonic generation (THG) emissions from the thin film of $Au(I)_6$ NCs when excited at 1300, 1400, 1500, and 1550 nm. Inset shows a schematic illustration of THG process in $Au(I)_6$ NCs. (e) Schematic illustration (top) and optical microscope image of the back gated WSe_2 field effect transistor. The inset shows the optical micrograph of the device after AuNC deposition. Reproduced from ref. 77 Copyright © 2023 Wiley-VCH. (g) A schematic of the LED device using Au_2Cu_6 NC. (h) Electroluminescence spectra of the device at 5, 7, and 10 V. (i) EQE *vs.* luminance curve. Reproduced with permission from ref. 95 Copyright © 2025 Wiley-VCH.

allows a combination of high harmonic generation and strong photoluminescence in NCs. Chandra *et al.* reported one of the first examples of ultrasmall AuNC displaying third harmonic generation and high photoluminescence (Fig. 3d–f).[97] The ultrasmall Au_6NC was stabilized with a rigid 6-(dibutylamino)-1,3,5-triazine-2,4-dithiol (TRZ) ligand, where all gold atoms are in the Au(I) state. The Au NC films showed intense third harmonic generation due to the centrosymmetric Au core. Due to the electron-accepting ground state properties, the NCs were utilized as p-type dopants in 2D WSe_2 field effect transistors (FETs). In a recent study, Rival *et al.* demonstrated the fabrication of bimetallic gold–copper nanocrystal (NC)-based light-emitting diodes (NC-LED) using a solution-processed technique (Fig. 3g–i).[95] The bimetallic NC $[Au_2Cu_6(Sadm)_6(DPPEO)_2]$, displayed superior photophysical and electroluminescent properties. The NCs are stabilized by 1-adamantanethiol (HSadm) and 1,2-bis(diphenylphosphino)ethane (DPPE). The partially oxidized bis(diphenylphosphino)ethane oxide (DPPEO) ligands promoted crystallization through strong C–H···O, and C–H···π interactions. The NC displayed a high photoluminescence quantum yield (PLQY) of 62% in its solid state. The NCs-LED fabricated without a host matrix showed a maximum brightness of 1246 cd m^{-2} and an external quantum yield (EQE) of 12.60%. The reported values are highest among solution-processed, non-doped NC-LEDs. This work highlights the importance of ligand engineering in developing high-performance, photothermally stable luminescent NC and NC-based devices.

Two-dimensional nanosheets

Schmid and Beyer reported the two-dimensional assembly of $Au_{55}(PPh_3)_{12}Cl_6$ NC in a biphasic system (Fig. 4a–c).[98] A solution of NC in dichloromethane was used to achieve a thin layer of NC-trapped dichloromethane at the water surface in the presence of water-soluble phase boundary modifying agents such as per-6-deoxy-6-thio-α-cyclodextrin or poly(vinylpyrrolidone) with careful consideration of the concentration. The per-6-deoxy-6-thio-α-cyclodextrin, due to the presence of multiple hydroxyl groups, allowed an amphiphilic nature with thiol moieties facing dichloromethane, interacting strongly with the NCs. The interactions observed in poly(vinylpyrrolidone) were mainly due to the hydrophobic nature of the polymer backbone and PPh_3 ligands. This resulted in a highly ordered assembly of Au_{55}NCs with hexagonally packed structures and cubic close-packed assemblies with inter-NC distances of 2.3 ± 0.1 nm (Fig. 4b and c). The monolayer was readily transferred to the substrates. The observed structures were similar irrespective of the nature and molecular weight of the modifying agents. However, this approach is delicate and depends on the stability of the dichloromethane layer. Due to the higher density of dichloromethane compared to water, achieving a large area layer was challenging. In a slightly modified approach, the formation of quasi-one-dimensional stripes of $Au_{55}(PPh_3)_{12}Cl_6$ was achieved (Fig. 4d).[99] In this approach, the dispersion of NCs in dichloromethane was allowed to form a monolayer at the air–water interface. The monolayer was transferred to the substrate by immersing it in water at a controlled withdrawal rate with an inclination angle of 20°. This modified Langmuir–Blodgett (LB) technique induced the formation of stripes (3–4 clusters) with a separation distance of 8 nm between the stripes and an inter-NC distance of 2.2–2.3 nm (Fig. 4e and f). Other approaches, including the use of isooctyl-substituted poly-(paraphenylenethinylen) (PPE-i-octyl) in CH_2Cl_2,[100] and nanolithographically patterned templates, have been used to achieve one-dimensional assemblies of $Au_{55}(PPh_3)_{12}Cl_6$ NCs.[101]

Selvam *et al.* reported the synthesis of AuNCs by decomposing CH_3AuPPh_3 precursor in *o*-xylene in the presence of mercapto acids such as 16-mercaptohexadecanoic acid (16-MHDA), 11-mercaptoundecanoic acid (11-MUDA), and 3-mercaptopropionic acid (3-MPA) as the capping agents.[102] The amphiphilic nature of mercaptoacids allowed the ready

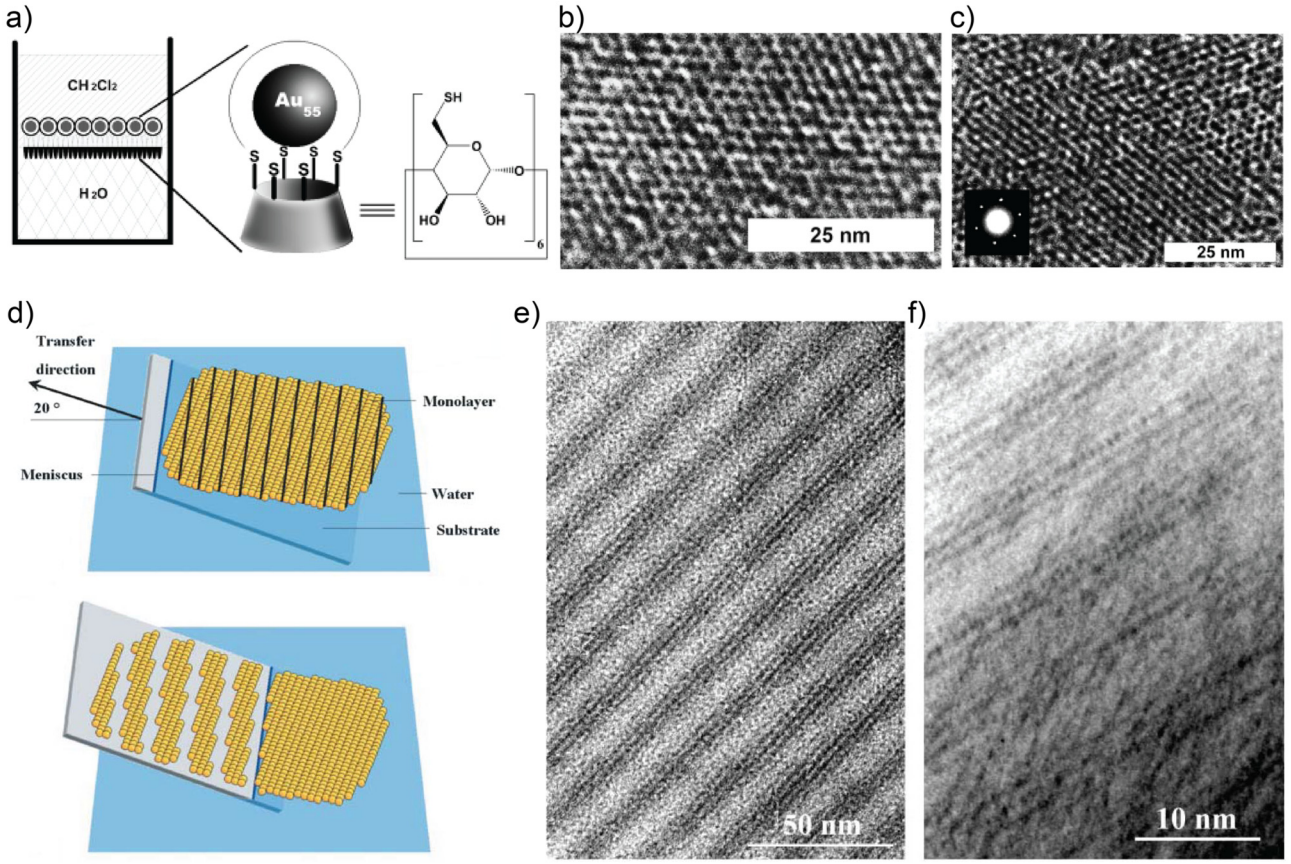

Fig. 4 NC-based 2D nanosheets. (a) Schematic illustration of $Au_{55}(PPh_3)_{12}Cl_6$ NC interaction at the phase boundary between water and dichloromethane and structure of per-6-deoxy-6-thio-α-cyclodextrin. (b) TEM image showing hcp arrays of $Au_{55}(PPh_3)_{12}Cl_6$ NCs with per-6-deoxy-6-thio-α-cyclodextrin. (c) TEM image showing hcp arrays of $Au_{55}(PPh_3)_{12}Cl_6$ NCs on PVP support. Reproduced with permission from ref. 98 Copyright © 2000 Wiley-VCH. (d) Schematic illustration showing monolayer and stripe formation of $Au_{55}(PPh_3)_{12}Cl_6$ NCs. (e) TEM image showing stripes and (f) Shows magnified TEM images of NC stripes with 3–4 rows of NCs. Reproduced from ref. 99 Copyright © 2001 Royal Society of Chemistry.

dispersion of clusters in aqueous and organic media. This biphasic solubility enabled both enhanced compatibility and stability in the solvent. Furthermore, the carboxylic acid dimerization led to inter-NC interaction, leading to nanosheets. The observed nanosheets showed aligned NCs with the size of individual NPs of 1.8 ± 0.2 nm. By tuning the ratio of the Au precursor to 16-MHDA, it was shown that the self-assembled sheets were predominantly observed when at 1 : 4 molar ratio of CH_3AuPPh_3 : 16-MHDA. The addition of amines to the reaction mixture perturbed the hydrogen bonding between the self-assembled clusters, resulting in smaller nanobelts. Furthermore, the ordered assembly of NCs were observed for ligands with longer alkyl chains (C16, C11) compared to the shorter chains (C3). The observed effect was attributed to the slightly higher hydrophilic nature and possible steric hindrance of shorter chain mercapto acids, which impede the ordered arrangement of NCs.

Temperature plays a significant role in influencing thermodynamic and kinetic aspects of nanocluster self-assembly, impacting the formation of mono- or multilayered 2D structures.[74,75] By altering the temperature, the enthalpic and entropic contributions within the system can be manipulated. At lower temperatures, the system favors minimizing free energy by enhancing cluster–cluster and cluster–solvent interactions, often leading to the formation of well-ordered, close-packed monolayers. Computational studies suggest that temperature can drive transitions between different structural motifs of gold nanoclusters.[75f] Higher temperatures provide nanoclusters with increased thermal energy, enhancing their diffusion and mobility, which can promote assembly. However, if reorganization is incomplete before complete solvent evaporation, this can lead to multilayered or defective structures. Temperature also influences solvent evaporation kinetics, as rapid evaporation at elevated temperatures may trap clusters in disordered or stacked configurations. In contrast, slower evaporation at lower temperatures enables more controlled, defect-free monolayer formation. Furthermore, Brownian motion increases at higher temperatures, enhancing nanocluster rearrangement and alignment at interfaces. However, excessive mobility without sufficient equilibration time may lead to random aggregation. Since supramolecular interactions among ligands largely govern self-assembly, temperature can modulate van der Waals, dipolar, and solvophobic interactions between clusters and at interfaces.

Wu *et al.* reported the assembly of dodecanethiol (DT) capped $Au_{15}DT_{15}$ NC into mono., few-, and multilayered nanosheets by utilizing inter-NC dipolar interactions. The NCs are prepared in dibenzyl ether (BE), which acts as a reducing agent as well as a capping agent (Fig. 5a–g).[103–105] The 2D nanostructures were produced by first producing 1D-oriented assemblies of NCs by annealing the BE solution at room temperature, followed by heating at 90 °C. The 2D structure displayed center-to-center inter-NC distances of 2.2 and 3.6 nm, respectively, in the *x* and *y* directions. Small angle XRD revealed a diffraction peak at 2.44° corresponding to *d* spacing of 3.6 nm that matched the *y*-direction. However, the peaks corresponding to 2.2 nm were not observed, indicating heterogeneity in NC along the *x*-direction. Brownian Dynamics (BD) simulations indicated that during self-assembly, DTs attain a new conformation and are redistributed preferentially along the *y* direction compared to the *x* direction. This results in anisotropic grafting density with 0.8 DTs per nm^2 in the *x* direction compared to 2.2 per nm^2 in the *y* direction, inducing anisotropic vdW attraction. Heating the BE solution at 140 °C resulted in the formation of multilayered 2D structures with 150 ± 20 nm width and 500–2000 nm in length due to the coalescence of small 2D structures. To produce monolayer assemblies, Au_{15} solution in BE was mixed with liquid Paraffin (LP) at a BE/LP v/v ratio of 1 : 7.5 followed by heating at 140 °C. Adding LP lowered the surface tension of BE, which acts as liquid exfoliation by limiting inter-layer interaction. This resulted in assembled structures of 200–300 nm in lateral width and up to 1000 nm in length. The sheet-like assemblies consisting of nanoclusters showed an inter-NC distance of 3.0 ± 0.3 nm, presumably due to the intercalation of dodecane thiol chains. Further, the AFM studies revealed that the thickness of sheet-like assemblies was 1.68 nm, which is less than the inter-nanocluster distance but slightly larger than the Au_{15} core size. This indicates a preferential distribution of DT chains at the interface of two immiscible liquids. These results were further supported using small angle X-ray diffraction (SAXRD) studies, which showed two *d* spacings of 3.6 nm and 3.2 nm, corresponding to intra-layer and inter-layer distances, respectively. This dual spacing pattern indicates a highly ordered arrangement. Yao *et al.* reported a phase transfer-driven ion-pairing approach to introduce amphiphilicity in AuNCs and their assembly into nanosheets (Fig. 5h–m).[106] The amphiphilicity was achieved by interacting 6-mercaptohexadecanoic acid (MHA) capped $Au_{25}(MHA)_{18}$ NC with cetyltrimethylammonium (CTA). The ion-pairing reaction between anionic $Au_{25}(MHA)_{18}$ NC and cationic CTA drives the phase transfer from the aqueous phase to the organic phase by modulating the polarity of the organic medium. This also offered control over the resulting complex $Au_{25}(MHA)_{18}@_xCTA$. The amphiphilicity results in the formation of micelles or vesicles at the air–liquid interface, eventually leading to film formation. These results state that nanoclusters and surfactants at interfaces can be arranged in a controlled manner to develop materials with specific functionality. Hou *et al.* reported the metal coordination-induced assembly of $Ag_6(mna)_6(NH_4)_6$ (mna = 2-mercapto nicotinic acid).[107] The single crystal X-ray structure of AgNCs revealed an octahedral silver core linked *via* argentophilic interactions protected by six mna^{2-} entities. The carboxylic acid groups, when interacted with divalent metal ions such as Ca^{2+} and Ba^{2+} resulted in nanosheets with enhanced luminescence. In the aqueous media, the aggregates would expose carboxylate moieties to water, facilitating the formation of 2D sheets within a lamellar structure. The individual AgNCs displayed yellow emission upon illumination at 365 nm with an absolute quantum yield of 2.26%. Upon self-assembly, the nanosheets and thin films showed orange emission with an enhanced quantum yield of 20.37%.

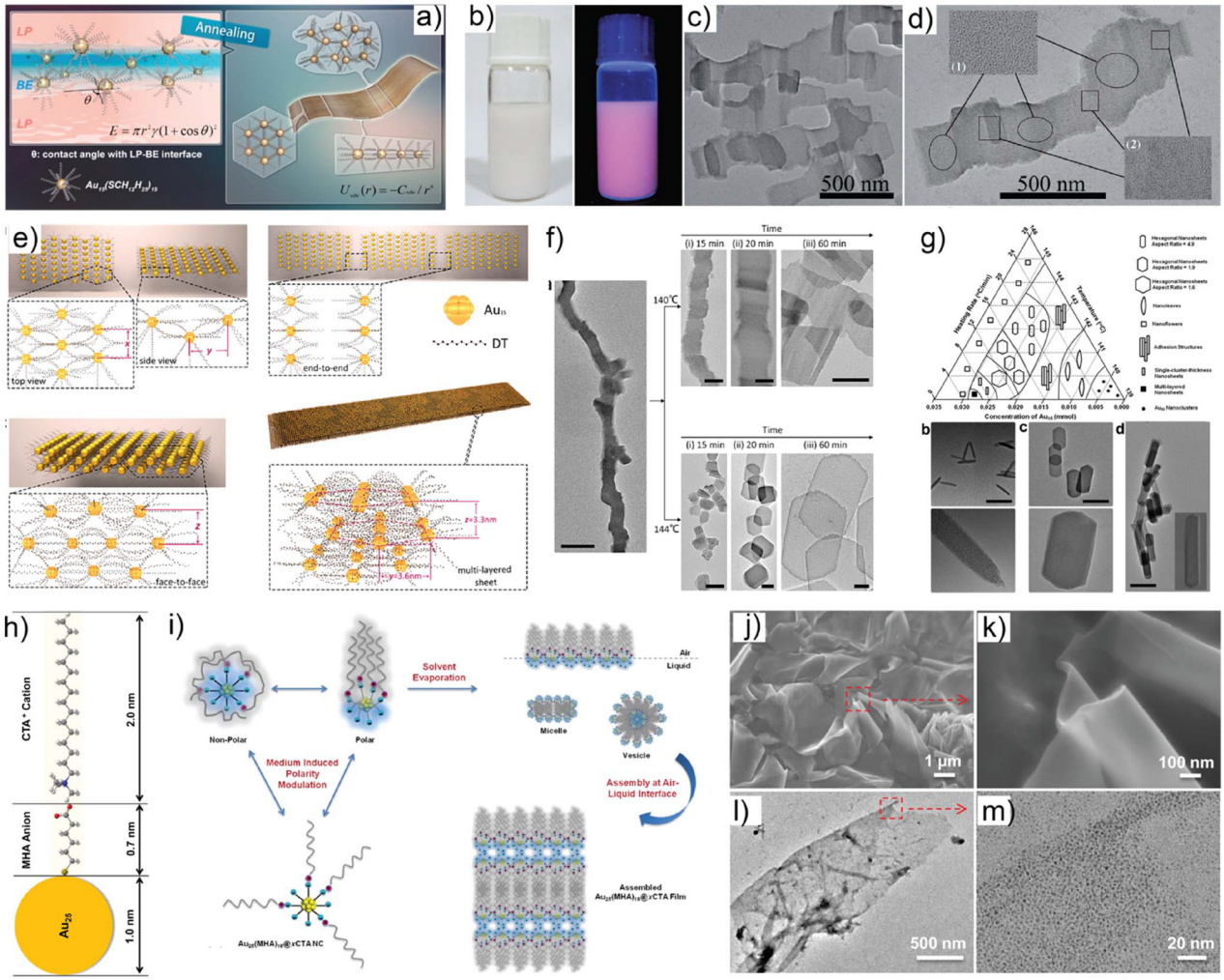

Fig. 5 (a) Directed self-assembly of NCs. Schematic illustration showing the directed self-assembly of Au_{15}NCs into monolayer nanosheets at the LP-BE interface. Reproduced with permission from ref. 105 Copyright © 2019 American Chemical Society. (b) Photographs showing optical (left) and PL (right) images of a dispersion of Au_{15} NC nanosheets in chloroform. (c and d) TEM images of nanosheets at different magnifications showing ordered and disordered domains. Reproduced with permission from ref. 103. Copyright © 2013 Wiley-VCH. (e) Schematic illustration showing the heating induced secondary assembly of small, isolated structures into multilayered nanosheets. (f) TEM images of time dependent evolution of secondary structures at 140 °C and 144 °C (scale bar: 200 nm). (g) Phase diagram showing dependence of self-assembled structure formation by changing the concentration of AuNCs, reaction temperature and heating rate and selected TEM images of different morphologies. Reproduced with permission from ref. 104. Copyright © 2015 American Chemical Society. (h) Schematic illustration showing the structure of $Au_{25}(MHA)_{18}@_xCTA$ NCs (x = 6–9). (i) Schematic representation of phase transfer driven assembly of $Au_{25}(MHA)_{18}@_xCTA$ NCs. (j and k) FE-SEM images and (l–m) TEM images of self-assembled $Au_{25}(MHA)_{18}@_xCTA$ NCs at the air–liquid interface. Reproduced with permission from ref. 106. Copyright © 2015 American Chemical Society.

The 2D nanosheets were sensitive to changes in the pH. The carboxylates undergo protonation at lower pH, breaking the metal coordination bonds. When nitric acid was added, it resulted in non-luminescent precipitates. Furthermore, neutralization at high pH using sodium hydroxide yielded well-defined hexagonal crystals with lateral lengths of up to tens of micrometers, exhibiting strong emission upon laser excitation (420 nm). Nakatani *et al.* synthesized AgNC-based 2D framework materials utilizing benzene-1,3,5-tricarboxylic acid tris-pyridin-4-ylamide (TPBTC) as a tridentate ligand.[108] Accordingly, the $[Ag_{12}(StBu)_6(CF_3COO)_6(TPBTC)_6]_n$ NC resulted in a luminescent porous framework structure with two-dimensional layers. The 2D layers are non-covalently linked to form a three-dimensional (3D) framework, generating uniaxial open channels. The porous network acts as a catalyst for the reduction of $[Fe(CN)_6]^{3-}$ using $NaBH_4$ in an aqueous medium. Paul *et al.* reported the self-assembly of L-phenylalanine and mercaptopropionic acid stabilized AuNCs using Zn coordination.[109] The self-assembly resulted in 2D nanosheets with a thickness varying from 3.8 ± 1.65 nm, featuring hexagonally arranged NCs, as confirmed by selected area electron diffraction (SAED) analysis. The resulting nanosheets exhibited luminescence with an emission maximum at 590 nm upon excitation at a wavelength of 330 nm. The nanosheets were investigated for their oxygen storage ability and

were found to have a capacity of 0.266 ± 0.004 mM g^{-1} of NCs at 20 °C and 20 bar. Furthermore, the nanosheets showed a decrease in luminescence intensity in the presence of oxygen and upon reducing the oxygen pressure, the luminescence was partially recovered. Therefore, such materials have the potential for oxygen storage and sensing applications.

There is growing interest in forming a NC-based framework materials that provides structural order and new possibilities in material design. Such systems enable the construction of 3D porous structures and 2D layers, offering enormous potential in catalysis, sensing, and energy storage applications. Dar *et al.* reported AgNC-based 2D and 3D metal organic frameworks of $[Ag_{12}(TBT)_7(TFA)_4(CH_3CN)_6]^+$ NC (TBT = tertiarybutylthiolate, TFA = trifluoroacetate).[110] The metal coordination in the presence of bidentate heterocyclic ligands resulted in AgNC-MOF $\{[Ag_{12}(TBT)_6(TFA)_6(pyz)_6]\cdot 2CH_3CN\}_n$ (pyz = pyrazine). The bidentate ligand coordinates with metal-rich silver chalcogenide ($Ag_{12}S_6$) clusters, resulting in a hexagonal planar structure that leads to infinite 2D frameworks with bright green luminescence. The 2D frameworks displayed an interlayer distance ~7.53 Å. Furthermore, due to weak van der Waals interactions and H···F hydrogen bonding between the layers, 2D nanosheets with lateral dimensions in the range of 0.156 μm were obtained using exfoliation.

Two-dimensional colloidal crystals

Nonappa *et al.* demonstrated the self-assembly of water-dispersible Au_{102}-*p*MBA_{44} (*p*MBA = *para*-mercaptobenzoic acid) NC in aqueous methanol to 2D colloidal crystals (Fig. 6).[111]

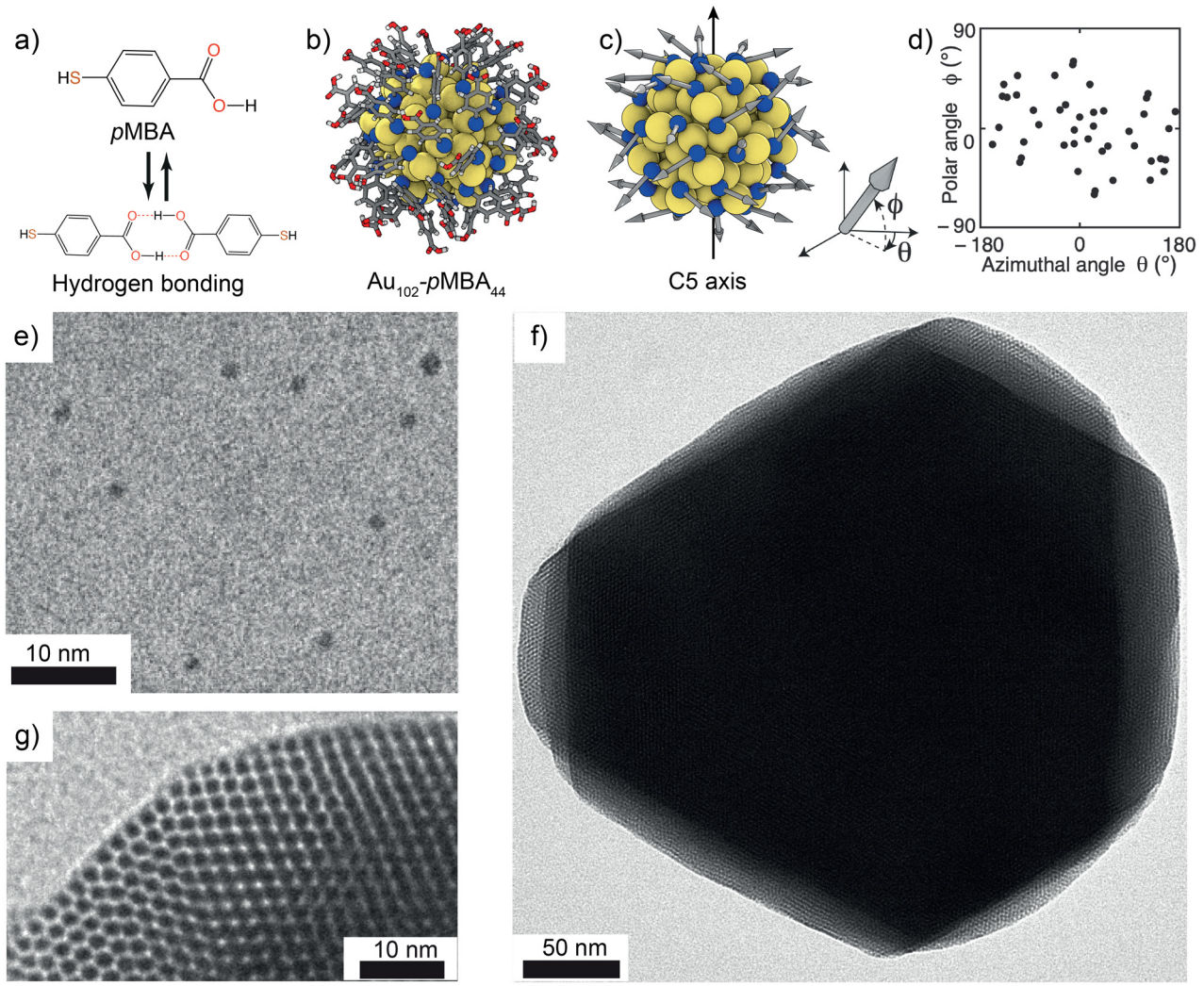

Fig. 6 Au NC-based 2D colloidal crystals. (a) Hydrogen bonding dimerization of the *p*-mercaptobenzoic acid (*p*MBA) ligands. (b) X-ray single crystal structure of Au_{102}-*p*MBA_{44} NC; gold (yellow), sulfur (blue), carbon (black), oxygen, and hydrogen (white). (c) and (d) The *p*MBA ligands are illustrated with arrows to determine their position, orientation, and location using a spherical coordinate system. (d) Shows the anisotropic distribution of ligands with a preference at the equatorial plane of an imaginary axis. (e) TEM image of individual Au_{102}-*p*MBA_{44} NCs dispersed in water. (f) TEM image of a self-assembled 2D colloidal crystal showing 3 layers of NCs. (g) TEM image showing the hexagonally close-packed NCs. Reproduced with permission from ref. 111 Copyright © 2016 Wiley-VCH.

By applying 3D spherical coordinate system to the single crystal X-ray structure, it was shown that in Au_{102}-*p*MBA$_{44}$ NC, *p*MBA ligands are preferentially oriented in the equatorial plane of an imaginary axis, suggesting the patchy and anisotropic distribution of ligands (Fig. 6b–d). The patchy and anisotropic distribution of ligands suggests the possibility of symmetry breaking in NCs, which can be exploited to fabricate lower-dimensional structures. The hydrogen-bonding dimerization of *p*MBA ligands was exploited to achieve 2D colloidal crystals. When all carboxylic acid groups are in the protonated form, the NC is dispersible in methanol. However, the NCs can be readily dispersed in water by partially deprotonating the carboxylic acid groups. More interestingly, the deprotonation of carboxylic acids results in a patchy distribution of negative charges due to the slight difference in the pKa values of the carboxylic acid groups. When an aqueous solution of partially deprotonated NCs was dialyzed against methanol, 2D colloidal crystals were formed with hexagonal close-packed arrays (Fig. 6f and g). The partial deprotonations prevent uncontrolled aggregation or random structures due to the electrostatic repulsion of negatively charged surfaces. Partially protonated carboxylic acid groups promote inter-nanocluster interaction through hydrogen bonding dimerization. Therefore, a fine equilibrium between electrostatic repulsion and attractive hydrogen bonding interactions is established, furnishing 2D colloidal crystals. Furthermore, adjusting the experimental conditions enabled the formation of defect-induced spherical and ellipsoidal capsids. Moreover, it has been further demonstrated that atomically precise NCs and narrow-size dispersed particles exhibit remarkably different self-assembly behaviors.[112] While this work provided crucial insights into patchy ligand distribution and symmetry breaking in NCs, certain limitations exist. For example, dialysis time should be carefully controlled to achieve 2D crystals, thereby avoiding a heterogeneous population of structures. Furthermore, the choice of solvents and self-assembly process may depend on the stability and ligand functional groups in NCs. Nevertheless, it provided the first evidence of solution state and template-free self-assembly of atomically precise NCs in aqueous conditions. Therefore, for large-scale structures, improved approaches and concepts are needed to achieve scalable structuring.

Among AgNCs, Na_4Ag_{44}-*p*MBA$_{30}$ is one of the most extensively studied molecules.[113] The X-ray single crystal structure of Na_4Ag_{44}-*p*MBA$_{30}$ shows *p*MBA ligands are arranged in bundles (Fig. 7a and b).

There are two types of ligand bundles, *viz.*, bundles of two (**L2**) and bundles of three (**L3**). There are six **L2** bundles that promote intra-layer hydrogen bonding. In contrast, the six **L3** bundles promote inter-layer hydrogen bonding. More importantly, all six **L2** bundles are positioned in the equatorial plane, resulting in 24 intralayer H-bonds. On the other hand, three of the **L3** bundles are distributed at the top and three at the bottom of an imaginary axis. Each of the **L3** bundle patches contributes 18 hydrogen bonds. This leads to an anisotropic distribution of the ligands (Fig. 7c and d). Due to the

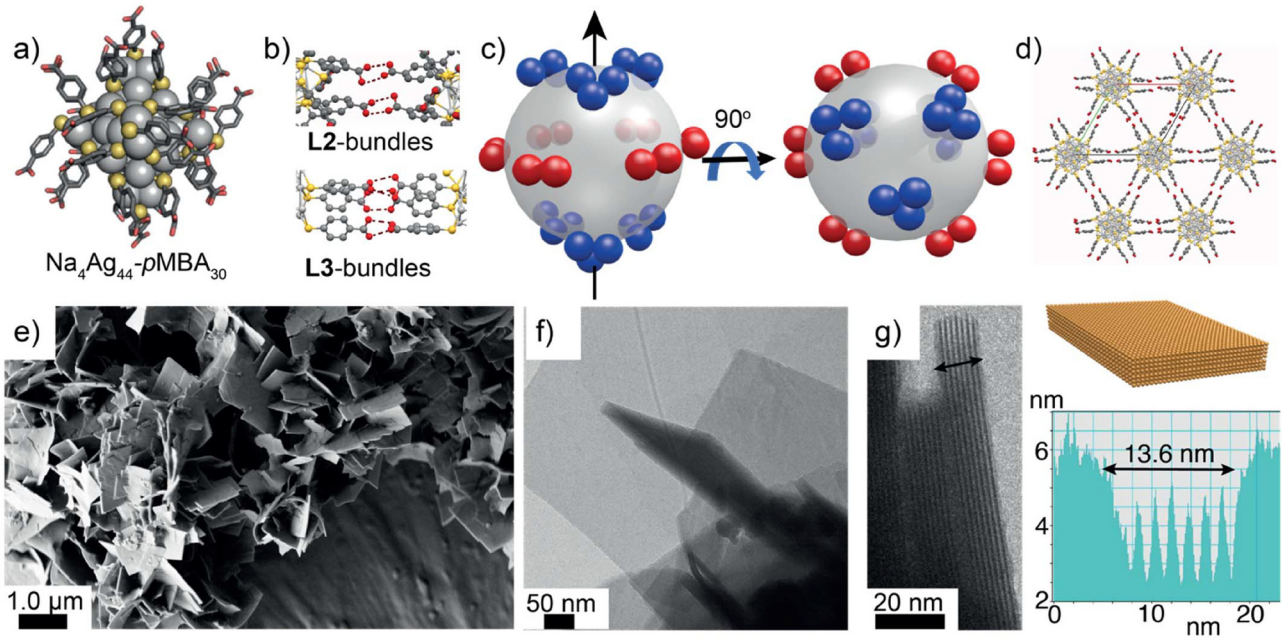

Fig. 7 Ag NC-based 2D colloidal crystals. (a) X-ray single crystal structure of Na_4Ag_{44}-*p*MBA$_{30}$ NC. (b) **L2** and **L3** ligand bundles in Na_4Ag_{44}-*p*MBA$_{30}$ NC showing hydrogen bonding dimerization. (c) Schematic illustration of **L2** bundles around the equatorial plane and (d) Selectively promoting intralayer hydrogen bonding and preventing interlayer hydrogen bonding allows 2D structures. (e) SEM image of 2D colloidal crystals of Na_4Ag_{44}-*p*MBA$_{30}$ NCs produced in methanol. (f) and (g) TEM images of 2D colloidal crystals suggest that the thickness of each layer corresponds to the diameter of one NC. Reproduced with permission from ref. 114 Copyright © 2022 Wiley-VCH.

well-defined ligand bundles and patchy hydrogen bonding interactions, Na_4Ag_{44}-pMBA$_{30}$ has been utilized to prepare nanoparticle-NC composite structures.[115] However, Na_4Ag_{44}-pMBA$_{30}$ NC is not stable under aqueous conditions. Therefore, the self-assembly procedure utilized for Au_{102}-pMBA$_{44}$ NC is incompatible with AgNCs. Som *et al.* utilized Na_4Ag_{44}-pMBA$_{30}$ NCs to prepare 2D colloidal crystals in alcoholic solvents.[114] This was achieved by adding a dispersion of the NC in *N*,*N*-dimethyl formamide to alcohols. A few layered 2D colloidal crystals were obtained for all tested lower alcohols (methanol, ethanol, *n*-propanol, and *n*-butanol). The resulting 2D crystals showed varying numbers of layers (1–8), with the thickness of each layer corresponding to the size of one nanoparticle (Fig. 7e–g). The 2D crystal formation in lower alcoholic solvents is attributed to their low viscosity, which accelerates assembly kinetics, resulting in phase separation and colloidal crystal formation.

Large-area membranes

Because of its patchy ligand bundles with directional hydrogen bonding, Na_4Ag_{44}-pMBA$_{30}$ NC has been utilized for composite film fabrication with anisotropic nanoparticles. Som *et al.* reported the Na_4Ag_{44}-pMBA$_{30}$-mediated assembly of tellurium nanowires (TeNW) into crossed bilayer structures at the air–water interface.[115] A mixture of Ag_{44}@TeNW in 1-butanol was placed on the surface of water in a petri dish and the evaporation of 1-butanol induced the assembly of NWs, resulting in a free-standing film with a crossed bilayer structure. Interestingly, the NWs aligned parallel to each other within a layer. The NWs displayed an unusual 81° angle between two layers, generating a woodpile-like structure and a woven fabric-like structure. The structure formation was driven by the anchoring of Ag_{44}NCs onto the TeNW surfaces through some of the carboxylate (–COO–) groups of ligands. Upon the evapor-

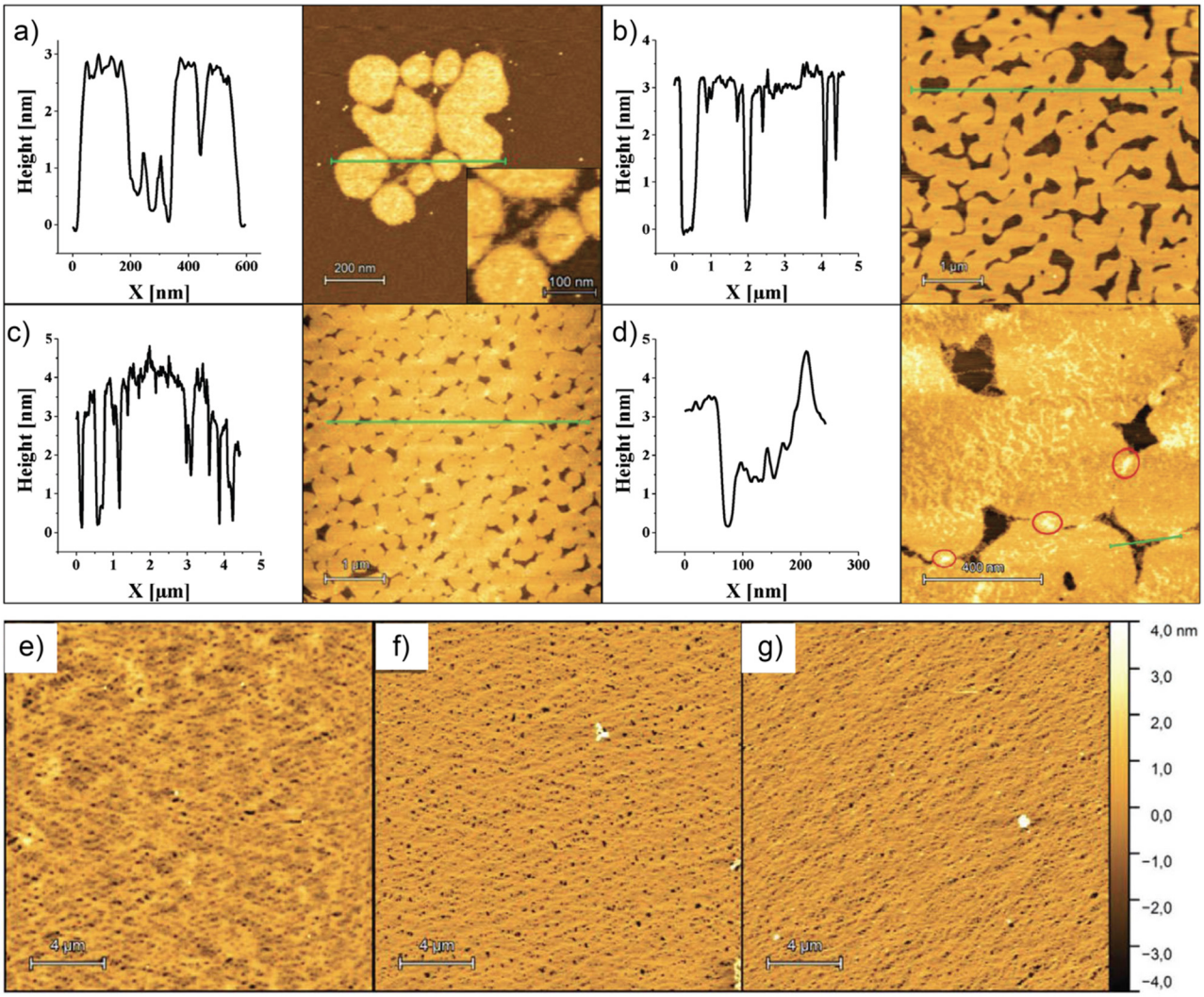

Fig. 8 Ultrathin films of NCs. (a) AFM height profile (left) image (right) of $Au_{38}(SC_2H_4Ph)_{24}$ NC films on mica substrate without compression. The height profiles and corresponding images after reaching a target pressure of (b) 9 mN m^{-1} and (c and d) 18 mN m^{-1}. (e, f and g) AFM images of $Au_{38}(SC_2H_4Ph)_{24}$ NC films on mica substrate after keeping at a target pressure of 18 mN m^{-1} for 3, 6 and 12 h, respectively. Reproduced with permission from ref. 116 Copyright © 2021 Wiley-VCH.

ation of 1-butanaol, the carboxylates not bound to TeNWs promote the hydrogen bonding between the clusters attached to neighboring TeNWs. The resulting film was transferred onto a PET (polyethylene terephthalate) substrate to fabricate the sensor. When subjected to bending, the device exhibited a change in electrical conductivity, suggesting potential use as an electronic skin for strain sensing. Swerczewski *et al.* utilized the Langmuir–Blodgett (LB) technique to fabricate ultrathin films of $Au_{38}(SC_2H_4Ph)_{24}$ NCs at an air–water interface (Fig. 8).[116] The film formation was achieved by placing a dispersion of AuNCs in dichloromethane/*n*-hexane (30 : 70) on the water surface in the LB trough. The film was transferred to a silicon or mica substrate. Using the LB isotherm and AFM studies, the evolution of the ultrathin films was studied. Film deposition on mica resulted in circular-shaped islands due to minimizing the Gibbs free energy of the system. The structure revealed heights of 2.75 nm (for fully interdigitated) and 4.12 nm (for AB stacks) for bilayers, and 3.63 and 6.18 nm for trilayers (Fig. 8a–d). Films without compression resulted in a bilayer of height 2.8 nm. Compression affects the structure and order (Fig. 8e–g). The Fast AFM results showed that the NCs were arranged in hexagonally close-packed arrays.

Despite recent progress in fabricating various 2D nanostructures, developing a highly precise monolayer membrane with reproducible structures, properties and mechanical properties remained a fundamental challenge. A majority of the 2D layered structures are heterogeneous, or multilayered membranes. In a recent study, Som *et al.* utilized Na_4Ag_{44}-*p*MBA_{30} NC to demonstrate the fabrication of large-area monolayer membranes (Fig. 9).[114] As discussed, Na_4Ag_{44}-*p*MBA_{30} NC resulted in 2D colloidal crystals when dispersed in lower alcohols such as methanol, ethanol, *n*-propanol and *n*-butanol. However, a clear dispersion was obtained when 1-pentanol was used. Furthermore, due to a longer alkyl chain, 1-pentanol is known to have low water solubility and form a transient solvent layer when placed on the water surface. These properties of 1-pentanol were exploited to fabricate large-area monolayer membranes. The membrane was formed at the air–water interface by introducing a dispersion of NCs in 1-pentanol onto the water surface, which was placed in a Petri dish (Fig. 9a).

The resulting transient layer trapped NCs, driving intralayer hydrogen bonding through carboxylic acid dimerization of **L2** bundles. Eventually, the 1-pentanol was dissolved in water, leaving the NC membrane intact on the surface. The monolayer membrane was readily transferred to different substrates without any pre-treatment or functionalization of the substrate (Fig. 9b and c). Alcohols, being protic polar solvents, mediate interactions between nanoclusters and ligands *via* their polar functional groups, stabilizing intermediate structures during self-assembly.[74,75g] By selecting alcohols with appropriate carbon chain lengths, their evaporation rates can be finely tuned, enabling sufficient time for nanoclusters to diffuse and reorganize into ordered structures before complete solvent evaporation. During evaporation, nanoclusters accumulate

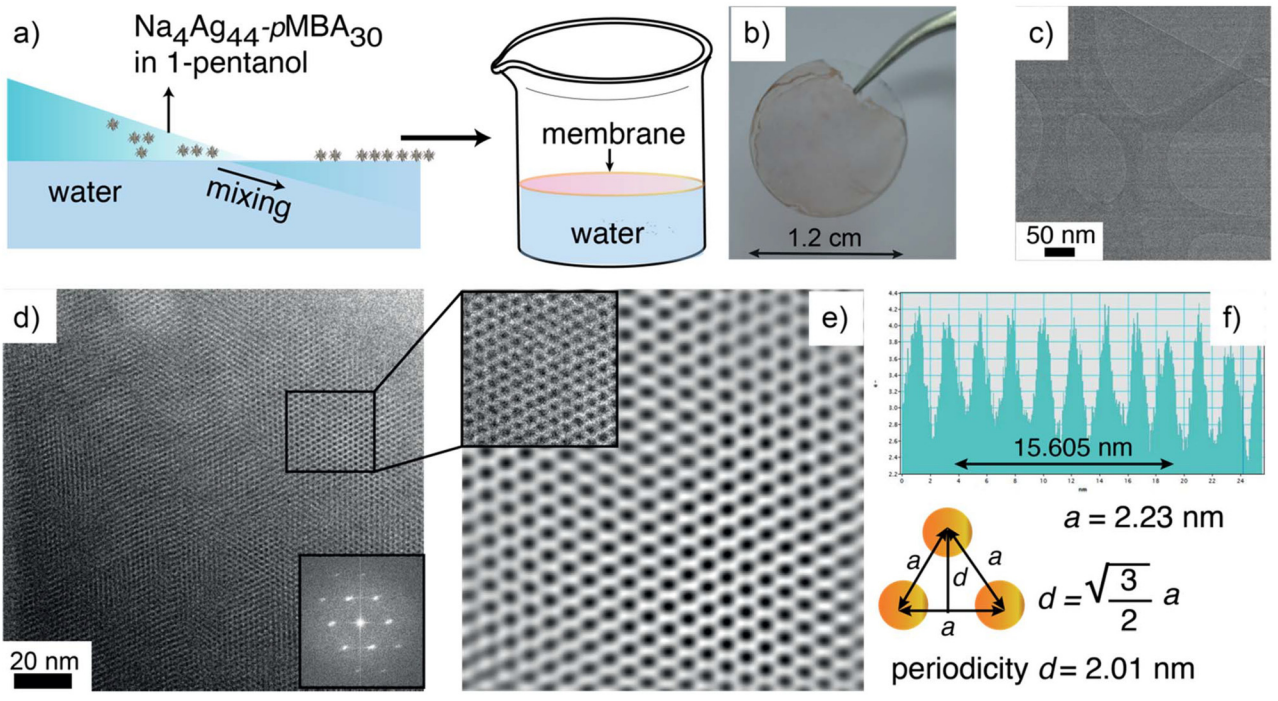

Fig. 9 NC-based large-area free-standing monolayer membranes. (a) Schematic illustration of NC-based large-area membrane fabrication using NCs trapped in a transient solvent layer. (b) Photograph of a Na4Ag44-*p*MBA30 NC membrane on a cover slip. (c) TEM image of the NC membrane stretched over a TEM grid with lacey carbon support film. (d) The TEM image shows the hexagonal close packing of NCs (the inset shows the FFT). (e) IFFT image of the selected area indicated in image c. (f) Profile shows inter-NC distance of 2.33 nm and periodicity of 2.01 nm. Reproduced with permission from ref. 114 Copyright © 2016 Wiley-VCH.

near the air–water interface, where close packing and ordered aggregation are promoted. Slower evaporation allows diffusion-driven rearrangement, favoring the formation of defect-free 2D crystals. In contrast, rapid evaporation may trap disordered aggregates, necessitating post-assembly treatment such as annealing to resolve defects. Due to their polar nature, alcohols can interact directly with the surface metal atoms of nanoclusters, thereby stabilizing exposed surfaces. This interaction may lead to metal core contraction and enhanced ligand bundling. Additionally, capillary forces act between clusters *via* meniscus formation during solvent loss, promoting cluster cohesion. Alcohols also help reduce interfacial energy, enabling the formation of close-packed monolayers at the interface.

The formation of a monolayer membrane was supported by high-resolution transmission electron microscopy imaging,

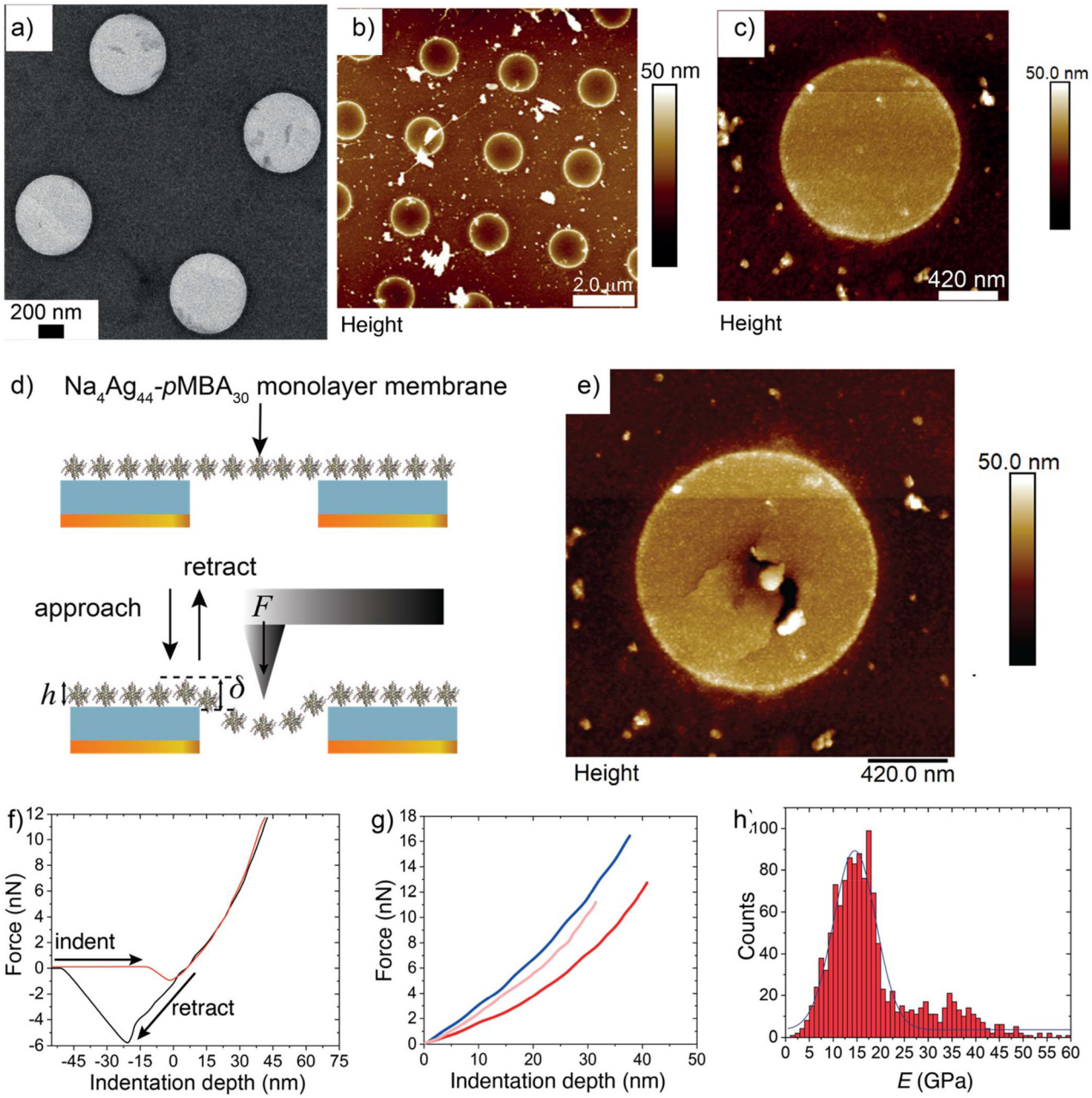

Fig. 10 Mechanical properties of monolayer membranes. (a) TEM images of the monolayer membrane stretched over a TEM grid with a holey carbon support film. (b) and (c) AFM images of the membrane. (d) A cartoon representation of the membrane deposited on top of the TEM grid and related AFM experimental setup. (e) AFM image of the membrane after many indentation cycles at different close spots. (f) A typical force-displacement curve suggests the elastic nature of the membrane. (g) Overlap of $F(\delta)$ curves recorded on three different holes covered with membranes. (h) Histogram showing the Young's modulus (E) values extracted by fitting the $F(\delta)$ curves. Reproduced with permission from ref. 114 Copyright © 2016 Wiley-VCH.

which revealed an inter-nanocluster interaction of 2.33 nm. Notably, the membrane retained the intrinsic properties of NCs, as supported using UV-vis spectroscopy. The membranes showed the characteristic absorption peaks observed for NCs dispersed in solution. More importantly, well-resolved Raman peaks were observed for monolayer membranes compared to those of a drop casted film of NCs. AFM images of membranes suspended on TEM grids with holy carbon support films also supported the monolayer nature (Fig. 10a–c)

Force–displacement curves recorded at the center of the membranes displayed consistent behavior under increasing loads from 10 nN up to ~16–18 nN, the maximum force the membranes could withstand before rupture (Fig. 10d–g). At small indentations, force varied linearly with displacement, while at larger indentations, a cubic relationship ($F \approx \delta^3$) emerged, enabling accurate extraction of Young's modulus (E). The membranes displayed a Young's modulus of 14.5 ± 0.2 GPa (Fig. 10h). This suggests that the atomic precision of the building blocks allows for reproducible mechanical properties with a narrow distribution. The narrow distribution of Young's modulus is attributed to a well-defined size, interacting patches and atomic-level precision of NCs. However, due to non-covalent interactions, these membranes display mechanical properties that are significantly lower than those of covalent 2D materials, such as graphene. Notably, the average Youngs modulus values are higher than those reported for alkanethiol and DNA-capped plasmonic nanoparticle membranes. This is attributed to the well-defined ligand bundles and hydrogen bonding interactions between the nanoclusters, which allow for better structural integrity. Unlike alkanethiol ligands, *p*MBA molecules are short and rigid with directional hydrogen bonding interactions. Furthermore, *p*MBA ligands do not induce ligand entanglement, unlike polymer membranes. Due to their atomically precise structure and small size, NCs create ultrasmall nanogaps, which can be utilized to generate strong and tunable electromagnetic fields for surface-enhanced Raman spectroscopy (SERS) signals in dye molecules. The Na_4Ag_{44}-*p*MBA_{30} membrane was tested for SERS detection of Amphotericin B, an antibiotic molecule dissolved in water. NC monolayer films showed the ability to detect as low as 2.5 μg mL^{-1} of Amp B. Whereas, at this concentration, the characteristic Raman peak was not observed in the case of a similar film containing polydispersed AgNPs or drop-casted films of AgNCs. In addition to its high sensitivity, the NC membrane also showed high reproducibility.

Conclusions

Noble metal nanoparticle-based self-assembled 2D nanostructures offer unique optoelectronic properties and mechanical performances. Therefore, they have emerged as one of the most promising candidates for application in nanodevices, sensors, catalysis, energy storage and flexible wearable devices. Despite the promise held by plasmonic nanoparticles, they suffer from limitations such as batch-to-batch variation, uncontrolled ligand density, aggregation tendencies, and a lack of directional interactions, leading to inconsistent and inhomogeneous structures. In contrast, due to their defined structure, composition, and stability, atomically precise noble metal nanoclusters have emerged as robust and modular building blocks for fabricating 2D materials. Their precision allows uniform and reproducible structures, addressing the challenges associated with larger plasmonic nanoparticles. While early approaches, such as electrostatic or evaporation-induced assembly, offered initial insights, they were often limited to quasi-2D structures within nanoscale domains. More recent advances, like multilayered nanosheets *via* directed assembly or solution-phase assembly exploiting anisotropic ligand patterns, demonstrate greater control, yet they demand fine-tuned experimental conditions and solvent compatibility. The choice of substrate and assembly method depends on the thermodynamics, kinetics, and nature of inter-nanocluster and nanocluster–substrate interactions. The substrate or method must provide an environment that facilitates the assembly and stabilization of nanoclusters. This involves matching the surface energy of the substrate with that of the nanoclusters and their ligands to reduce interfacial free energy and promote ordered packing. Solid substrates, especially those with tailored surface functional groups, can influence spatial arrangement by guiding cluster positioning. The rate of deposition and nanocluster mobility on the substrate surface impact the quality of the final assembly. For instance, slow evaporation on a solid substrate allows nanoclusters sufficient time to diffuse and self-assemble into defect-free monolayers, whereas rapid deposition may lead to disordered trapping. At air–liquid or liquid–liquid interfaces, nanoclusters retain mobility until solvent evaporation or interfacial trapping occurs, allowing for dynamic reorganization. Solvent-based methods promote assembly of nanoclusters through capillary action, evaporation dynamics, and ligand–ligand or ligand–solvent interactions. The presence of a liquid phase allows clusters to rearrange and even enable the reorganization of defects. Solid-supported assemblies tend to offer higher stability as the immobilized nanoclusters are less prone to further aggregation or redissolution. In contrast, solvent-based or interfacial assemblies may be more sensitive to environmental changes, such as evaporation or interface disturbance. However, they also allow for flexibility in reorganization and post-assembly defect correction before final structure formation. A careful and systematic optimization of self-assembly parameters can yield macroscopic, elastic monolayer membranes that not only preserve the intrinsic functionalities of individual nanoclusters but also display superior mechanical integrity and optical responses. The nanocluster-based 2D materials have shown promising results in sensing gas molecules, volatile organic compounds, and antibiotics, with high sensitivity and reproducibility, and they even displayed enhanced photoluminescence. While the nanocluster-based 2D nanomaterials have shown enormous potential, achieving scalable and systematic fabrication of such 2D nanostructures remains a critical challenge. However, the growing library of

nanocluster solid-state structures offers a valuable platform for predictive design of next-generation functional 2D materials. Therefore, in the future, the integration of computational simulations, machine learning, and artificial intelligence-driven design holds the promise to revolutionize how we conceptualize, engineer, and apply nanocluster-based 2D materials for emerging applications.

Author contributions

The manuscript was written with contributions from all authors.

Conflicts of interest

There are no conflicts to declare.

Data availability

No primary research results, software or code have been included and no new data were generated or analysed as part of this review.

Acknowledgements

The Research Council of Finland for project funding (No. 352900) and Flagship program on Photonics Research and Innovation (PREIN) are acknowledged.

References

1 M. Zeng, Y. Xiao, J. Liu, K. Yang and L. Fu, *Chem. Rev.*, 2018, **118**, 6236–6296.
2 K. S. Novoselov, A. K. Geim, S. V. Morozov, D. Jiang, Y. Zhang, S. V. Dubonos, I. V. Grigorieva and A. A. Firsov, *Science*, 2004, **306**, 666–669.
3 X. Fan, F. Forsberg, A. D. Smith, S. Schröder, S. Wagner, H. Rödjegård, A. C. Fischer, M. Östling, M. C. Lemme and F. Niklaus, *Nat. Electron.*, 2019, **2**, 394–404.
4 Y. Wang, X. Li, Z. Jiang, L. Tong, W. Deng, X. Gao, X. Huang, H. Zhou, Y. Yu, L. Ye, X. Xiao and X. Zhang, *Nat. Commun.*, 2021, **12**, 5076.
5 R. Raccichini, A. Varzi, S. Passerini and B. Scrosati, *Nat. Mater.*, 2015, **14**, 271–279.
6 A. J. Clancy, H. Au, N. Rubio, G. O. Coulter and M. S. P. Shaffer, *Dalton Trans.*, 2020, **49**, 10308–10318.
7 L. H. Li, E. J. G. Santos, T. Xing, E. Cappelluti, R. Roldán, Y. Chen, K. Watanabe and T. Taniguchi, *Nano Lett.*, 2015, **15**, 218–223.
8 S. Manzeli, D. Ovchinnikov, D. Pasquier, O. V. Yazyev and A. Kis, *Nat. Rev. Mater.*, 2017, **2**, 17033.
9 (*a*) A. Vaccari, *Catal. Today*, 1998, **41**, 53–71; (*b*) Z. Chen, Q. Fan, M. Huang and H. Cölfen, *CrystEngComm*, 2022, **24**, 4639–4655.
10 (*a*) J. Zhu, P. Xiao, H. Li and S. A. C. Carabineiro, *ACS Appl. Mater. Interfaces*, 2014, **6**, 16449–16465; (*b*) J. Liu, H. Wang and M. Antonietti, *Chem. Soc. Rev.*, 2016, **45**, 2308–2326.
11 (*a*) M. E. Dávila and G. Le Lay, *Mater. Today Adv.*, 2022, 100312; (*b*) H. Oughaddou, H. Enriquez, M. R. Tchalala, H. Yildirim, A. J. Mayne, A. Bendounan, G. Dujardin, M. A. Ali and A. Kara, *Prog. Surf. Sci.*, 2015, **90**, 46–83.
12 (*a*) Y. Gogotsi and B. Anasori, *ACS Nano*, 2019, **13**, 8491–8494; (*b*) Y. Gogotsi and Q. Huang, *ACS Nano*, 2021, **15**, 5775–5780.
13 P. Kissel, D. J. Murray, W. J. Wulftange, V. J. Catalano and B. T. King, *Nat. Chem.*, 2014, **6**, 774–778.
14 C. Shi, M. S. Duyar, X. Wang, S. Ye, M. Hu and J. Liu, *FlatChem*, 2021, 100287.
15 (*a*) O. Jurček, Nonappa, E. Kalenius, P. Jurček, J. M. Linnanto, R. Puttreddy, H. Valkenier, N. Houbenov, M. Babiak, M. Peterek, A. P. Davis, R. Marek and K. Rissanen, *Cell Rep. Phys. Sci.*, 2021, **2**, 100303; (*b*) K. Koner, H. S. Sasmal, D. Shetty and R. Banerjee, *Angew. Chem., Int. Ed.*, 2024, **63**, e202406418.
16 Y. Chen, Z. Fan, Z. Zhang, W. Niu, C. Li, N. Yang, B. Chen and H. Zhang, *Chem. Rev.*, 2018, **118**, 6409–6455.
17 F. Xia, H. Wang, D. Xiao, M. Dubey and A. Ramasubramanianm, *Nat. Photonics*, 2014, **8**, 899–907.
18 D. Deng, K. Novoselov, Q. Fu, N. Zheng, Z. Tian and X. Bao, *Nat. Nanotechnol.*, 2016, **11**, 218–230.
19 (*a*) E. Pomerantseva and Y. Gogotsi, *Nat. Energy*, 2017, **2**, 17089; (*b*) P. Zhang, F. Wang, M. Yu, X. Zhuang and X. Feng, *Chem. Soc. Rev.*, 2018, **47**, 7426–7451.
20 (*a*) P. Srikrishnarka, J. Haapasalo, J. P. Hinestroza, Z. Sun and Nonappa, *Small Sci.*, 2024, **4**, 2300358; (*b*) Y. Sun, W. He, C. Jiang, J. Li, J. Liu and M. Liu, *Nano-Micro Lett.*, 2025, **17**, 109.
21 S. Roy, X. Zhang, A. B. Puthirath, A. Meiyazhagan, S. Bhattacharyya, M. M. Rahman, G. Babu, S. Susarla, S. K. Saju, M. K. Tran, L. M. Sassi, M. A. S. R. Saadi, J. Lai, O. Sahin, S. M. Sajadi, B. Dharmarajan, D. Salpekar, N. Chakingal, A. Baburaj, X. Shuai, A. Adumbumkulath, K. A. Miller, J. M. Gayle, A. Ajnsztajn, T. Prasankumar, V. V. J. Harikrishnan, V. Ojha, H. Kannan, A. Z. Khater, Z. Zhu, S. A. Iyengar, P. A. da Silva Autreto, E. F. Oliveira, G. Gao, A. G. Birdwell, M. R. Neupane, T. G. Ivanov, J. Taha-Tijerina, R. M. Yadav, S. Arepalli, R. Vajtai and P. M. Ajayan, *Adv. Mater.*, 2021, **33**, 2101589.
22 Y. Huang, Y.-H. Pan, R. Yang, L.-H. Bao, L. Meng, H.-L. Luo, Y.-Q. Cai, G.-D. Liu, W.-J. Zhao, Z. Zhou, L.-M. Wu, Z.-L. Zhu, M. Huang, L.-W. Liu, L. Liu, P. Cheng, K.-H. Wu, S.-B. Tian, C.-Z. Gu, Y.-G. Shi, Y.-F. Guo, Z.-G. Cheng, J.-P. Hu, L. Zhao, G.-H. Yang, E. Sutter, P. Sutter, Y.-L. Wang, W. Ji, X.-J. Zhou and H.-J. Gao, *Nat. Commun.*, 2020, **11**, 2453.

23 J. N. Coleman, M. Lotya, A. O'Neill, S. D. Bergin, P. J. King, U. Khan, K. Young, A. Gaucher, S. De, R. J. Smith, I. V. Shvets, S. K. Arora, G. Stanton, H.-Y. Kim, K. Lee, G. T. Kim, G. S. Duesberg, T. Hallam, J. J. Boland, J. J. Wang, J. F. Donegan, J. C. Grunlan, G. Moriarty, A. Shmeliov, R. J. Nicholls, J. M. Perkins, E. M. Grieveson, K. Theuwissen, D. W. McComb, P. D. Nellist and V. Nicolosi, *Science*, 2011, **331**, 568–571.

24 (*a*) K. R. Paton, E. Varrla, C. Backes, R. J. Smith, U. Khan, A. O'Neill, C. Boland, M. Lotya, O. M. Istrate, P. King, T. Higgins, S. Barwich, P. May, P. Puczkarski, I. Ahmed, M. Moebius, H. Pettersson, E. Long, J. Coelho, S. E. O'Brien, E. K. McGuire, B. M. Sanchez, G. S. Duesberg, N. McEvoy, T. J. Pennycook, C. Downing, A. Crossley, V. Nicolosi and J. N. Coleman, *Nat. Mater.*, 2014, **13**, 624–630; (*b*) C.-X. Hu, Y. Shin, O. Read and C. Casiraghi, *Nanoscale*, 2021, **13**, 460–484.

25 P. Chavalekvirat, W. Hirunpinyopas, K. Deshsorn, K. Jitapunkul and P. Iamprasertkun, *Precis. Chem.*, 2024, **2**, 300–329.

26 X. S. Li, W. W. Cai, J. An, S. Kim, J. Nah, D. Yang, R. Piner, A. Velamakanni, I. Jung, E. Tutuc, S. K. Banerjee, L. Colombo and R. S. Ruoff, *Science*, 2009, **324**, 1312–1314.

27 C. Muratore, A. A. Voevodin and N. Glavin, *Thin Solid Films*, 2019, **688**, 137500.

28 C. Liu, T. Liu, Z. Zhang, Z. Sun, G. Zhang, E. Wang and K. Liu, *Nat. Nanotechnol.*, 2024, **19**, 907–918.

29 S. M. George, *Chem. Rev.*, 2010, **110**, 111–131.

30 S. Xu and Q. Zhang, *Mater. Today Energy*, 2021, **20**, 100635.

31 Q. Gu, J. Zha, C. Chen, X. Wang, W. Yao, J. Liu, F. Kang, J. Yang, Y. Y. Li, D. Lei, Z. Tang, Y. Han, C. Tan and Q. Zhang, *Adv. Mater.*, 2024, **36**, e2306414.

32 Q. Gu, X. Lu, C. Chen, X. Wang, F. Kang, Y. Y. Li, Q. Xu, J. Lu, Y. Han, W. Qin and Q. Zhang, *Angew. Chem., Int. Ed.*, 2024, **63**, e202409708.

33 H. Zhang, M. Yang, Q. Wu, J. Xue and H. Liu, *Angew. Chem., Int. Ed.*, 2025, **64**, e202424768.

34 J. Wu, S. Zhang, Q. Gu and Q. Zhang, *FlexMat*, 2024, **1**, 160–172.

35 Y. Ma, B. Li and S. Yang, *Mater. Chem. Front.*, 2018, **2**, 456–467.

36 H. Liu, H. Tang, M. Fang, W. Si, Q. Zhang, Z. Huang, L. Gu, W. Pan, J. Yao, C. Nan and H. Wu, *Adv. Mater.*, 2016, **28**, 8170–8176.

37 K. Huang, J. Hou, Q. Zhang, G. Ou, D. Ning, N. Hussain, Y. Xu, B. Ge, K. Liu and H. Wu, *Chem. Commun.*, 2018, **54**, 160–163.

38 A. Funatsu, H. Tateishi, K. Hatakeyama, Y. Fukunaga, T. Taniguchi, M. Koinuma, H. Matsuura and Y. Matsumoto, *Chem. Commun.*, 2014, **50**, 8503–8506.

39 R. D. Piner, J. Zhu, F. Xu, S. H. Hong and C. A. Mirkin, *Science*, 1999, **283**, 661–663.

40 F. Wang, Z. Wang, T. A. Shifa, Y. Wen, F. Wang, X. Zhan, Q. Wang, K. Xu, Y. Huang, L. Yin, C. Jiang and J. He, *Adv. Funct. Mater.*, 2017, **27**, 1603254.

41 L. M. Liz-Marzán and M. Grzelczak, *Science*, 2017, **356**, 1120–1121.

42 Y. Xiong, H. Wu, Y. Cheng, M. Shao, Y. Wang, J. Zhou, F. Hao, F. Liu, L. Guo, X. Meng, C. Wang, G. Wang, J. Wang, M. Wang, Y. Ma and Z. Fan, *Chem. Mater.*, 2025, **37**, 10095–10104.

43 H. Guan, C. Harris and S. Sun, *Acc. Chem. Res.*, 2023, **56**, 1591–1601.

44 S. Ye, A. P. Brown, A. C. Stammers, N. H. Thomson, J. Wen, L. Roach, R. J. Bushby, P. L. Coletta, K. Critchley, S. D. Connell, A. F. Markham, R. Brydson and S. D. Evans, *Adv. Sci.*, 2019, **6**, 1900911.

45 X. Cui, F. Qin, Q. Ruan, X. Zhuo and J. Wang, *Adv. Funct. Mater.*, 2018, **28**, 1705516.

46 L. Chen, F. Ji, Y. Xu, L. He, Y. Mi, F. Bao, B. Sun, X. Zhang and Q. Zhang, *Nano Lett.*, 2014, **14**, 7201–7206.

47 C. M. Payne, D. E. Tsentalovich, D. N. Benoit, L. J. E. Anderson, W. Guo, V. L. Colvin, M. Pasquali and J. H. Hafner, *Chem. Mater.*, 2014, **26**, 1999–2004.

48 Y. Yue and Y. Norikane, *Nat. Commun.*, 2020, **11**, 568.

49 H. L. Qin, D. Wang, Z. L. Huang, D. M. Wu, Z. C. Zeng, B. Ren, K. Xu and J. Jin, *J. Am. Chem. Soc.*, 2013, **135**, 12544–12547.

50 S. K. Krishnan, R. Esparza, F. J. Flores-Ruiz, E. Padilla-Ortega, G. Luna-Bárcenas, I. C. Sanchez and U. Pal, *ACS Omega*, 2018, **3**, 12600–12608.

51 Y. Fan, Y. Ren, Y. Fang and M. Wu, *Micro Nano Lett.*, 2014, **9**, 726–730.

52 (*a*) S.-H. Yu, R. O'Reilly, L. Jiang and N. A. Kotov, *Acc. Chem. Res.*, 2022, **55**, 1783–1784; (*b*) A. Rao, S. Roy, V. Jain and P. P. Pillai, *ACS Appl. Mater. Interfaces*, 2023, **15**, 25248–25274.

53 Nonappa, *Chem. Commun.*, 2023, **59**, 13800–13819.

54 P. K. Jain, X. Huang, I. H. El-Sayed and M. A. El-Sayed, *Acc. Chem. Res.*, 2008, **41**, 1578–1586.

55 N. A. Kotov and P. S. Weiss, *ACS Nano*, 2014, **8**, 3101–3103.

56 (*a*) R. Sardar, A. M. Funston, P. Mulvaney and R. W. Murray, *Langmuir*, 2009, **25**, 13840–13851; (*b*) S. Zhang, G. Leem, L. Srisombat and T. R. Lee, *J. Am. Chem. Soc.*, 2008, **130**, 113–120; (*c*) C. S. Weisbecker, M. V. Merritt and G. M. Whitesides, *Langmuir*, 1996, **12**, 3763–3772.

57 K. E. B. Doncom, L. D. Blackman, D. B. Wright, M. I. Gibson and R. O'Reilly, *Chem. Soc. Rev.*, 2017, **46**, 4119–4134.

58 S. Shrestha, B. Wang and P. Dutta, *Adv. Colloid Interface Sci.*, 2020, **279**, 102162.

59 X. Zhang, L. Lv, L. Ji, G. Guo, L. Liu, D. Han, B. Wang, Y. Tu, J. Hu, D. Yang and A. Dong, *J. Am. Chem. Soc.*, 2016, **138**, 3290–3293.

60 L. Chen, B. Su and L. Jang, *Chem. Soc. Rev.*, 2019, **48**, 8–21.

61 X. Xue, K. Liu and E. P. Furlani, *J. Phys. Chem. C*, 2017, **121**, 9489–9496.

62 S. Cheng and G. S. Grest, *ACS Macro Lett.*, 2016, **5**, 694–698.

63 P. Katiyar and J. K. Singh, *J. Chem. Phys.*, 2019, **150**, 044708.
64 T. Ramachandran, A. Ali, F. A. Deader, H. Shafeekali, L. Zheng, H. Butt and M. Rezeq, *Langmuir*, 2025, **41**, 1271–1280.
65 B. C. Marchi and S. Keten, *Front. Mater.*, 2019, **6**, 174.
66 (*a*) T. P. Bignioni, X.-M. Lin, T. T. Nguyen, E. I. Crowin, T. A. Witten and H. M. Jaeger, *Nat. Mater.*, 2006, **5**, 265; (*b*) A. Desireddy, C. P. Joshi, M. Sestak, S. Little, S. Kumar, N. J. Podraza, S. Masillac, R. W. Collins and T. P. Bigioni, *Thin Solid Films*, 2011, **519**, 6077–6084; (*c*) A. Dong, J. Chen, P. M. Vora, J. M. Kikkawa and C. B. Murray, *Nature*, 2010, **266**, 474–477; (*d*) H. Duan and K. K. Berggren, *Nano Lett.*, 2010, **10**, 3710–3716.
67 K. E. Mueggenburg, X.-X. Lin, R. H. Goldsmith and H. M. Jaeger, *Nat. Mater.*, 2007, **6**, 656.
68 (*a*) W. J. Cho, Y. Kim and J. K. Kim, *ACS Nano*, 2012, **6**, 249–255; (*b*) F. Alibart, S. Pleutin, D. Guérin, C. Novembre, S. Lenfant, K. Lmimouni, C. Gamrat and D. Vuillaume, *Adv. Funct. Mater.*, 2010, **22**, 330–337.
69 W. Cheng, M. J. Campolongo, J. J. Cha, S. J. Tan, C. C. Umbach, D. A. Muller and D. Luo, *Nat. Mater.*, 2009, **8**, 519.
70 A. Raveendran and M.-V. Meli, *ACS Omega*, 2017, **2**, 4411.
71 C. Klinke, *Europhys. Lett.*, 2017, **119**, 36002.
72 (*a*) H. Häkkinen, *Nat. Chem.*, 2012, **4**, 443–455; (*b*) M. F. Matus and H. Häkkinen, *Nat. Rev. Mater.*, 2023, **8**, 372–389.
73 (*a*) L. Malatesta, L. Naldini, G. Simonetta and F. Cariat, *Chem. Commun.*, 1965, 212–213; (*b*) L. Naldini, F. Cariati, G. Simonetta and L. Malatesta, *Chem. Commun.*, 1966, 647–648; (*c*) M. McPartlin and R. Mason, *J. Chem. Soc. D*, 1969, 334; (*d*) P. A. Bartlett and B. B. S. J. Sanger, *J. Am. Chem. Soc.*, 1978, 5085.
74 (*a*) R. Jin, H. Qian, Z. Wu, Y. Zhu, M. Zhu, A. Mohanty and N. Garg, *J. Phys. Chem. Lett.*, 2010, **1**, 2903–2910; (*b*) Y. Pei and X. C. Zeng, *Nanoscale*, 2012, **4**, 4054–4072; (*c*) Z. Wu and R. Jin, *Atomically Precise Metal Nanoclusters*, Springer International Publishing, Cham, 2021, p. 31; (*d*) *Protected Metal Clusters from Fundamentals to Applications in Frontiers of Nanoscience*, ed. T. Tsukuda and H. Häkkinen, Elsevier Inc., 2015, pp. 1–358; (*e*) *Atomically Precise Metal Nanoclusters*, ed. T. Pradeep, Elsvier Inc., 2022, pp. 1–643; (*f*) R. Jin and D. Jiang, *Atomically Precise Nanochemistry*, Wiley-VCH, 2023, pp. 1–528; (*g*) E. Banach and T. Bürgi, *Helv. Chim. Acta*, 2022, **105**, e202100186; (*h*) S. Kolay, D. Bain, S. Maity, A. Devi, A. Patra and R. Antoine, *Nanomaterials*, 2022, **12**, 544.
75 (*a*) H. Häkkinen, *Chem. Soc. Rev.*, 2008, **37**, 1847; (*b*) H. Häkkinen, M. Walter and H. Grönbeck, *J. Phys. Chem. B*, 2006, **110**, 9927–9931; (*c*) M. Walter, J. Akola, O. Lopez-Acevedo, P. D. Jadzinsky, G. Calero, C. J. Ackerson, R. L. Whetten, H. Grönbeck and H. Häkkinen, *Proc. Natl. Acad. Sci. U. S. A.*, 2008, **105**, 9157–9162; (*d*) C. M. Aikens, *J. Phys. Chem. Lett.*, 2011, **2**, 99–104; (*e*) M. Taylor and G. Mpourmpakis, *Nat. Commun.*, 2017, **8**, 15988; (*f*) M. Settem, R. Ferrando and A. Giacomello, *Nanoscale*, 2022, **14**, 939–952; (*g*) D. M. Chevrier, B. E. Conn, B. Li, D.-E. Jiang, T. P. Bigioni, A. Chatt and P. Zhang, *ACS Nano*, 2020, **14**, 8433–8441.
76 (*a*) K. R. Krishnadas, A. Ghosh, A. Baksi, I. Chakraborty, G. Natarajan and T. Pradeep, *J. Am. Chem. Soc.*, 2016, **138**, 140–148; (*b*) P. Bose, K. K. Ramankutty, P. Chakraborty, E. Khatuna and T. Pradeep, *Nanoscale*, 2024, **16**, 1446–1470; (*c*) J. Roy, B. Mondal, G. Vishwakarma, Nonappa, N. V. Sridharan, P. Krishnamurthi and T. Pradeep, *Nanoscale*, 2023, **15**, 8225–8234; (*d*) A. Chakraborty, S. Manna, B. Mondal, M. Bodiuzzaman, A. Nagar, S. Chowdhury, T. Nayak, Nonappa and T. Pradeep, *Small*, 2025, **21**, 2409784; (*e*) P. Bose, P. Chakraborty, J. S. Mohanty, Nonappa, A. R. Chowdhuri, E. Khatun, T. Ahuja, A. Mahendranath and T. Pradeep, *Nanoscale*, 2020, **12**, 22116–22128; (*f*) P. Bose, P. Srikrishnarka, M. Paatelainen, Nonappa, A. R. Kini, A. Som and T. Pradeep, *Nanoscale*, 2025, **17**, 803–812; (*g*) P. Bose, J. Roy, V. Khokhar, B. Mondal, G. Natarajan, S. Manna, V. Yadav, A. Nyayban, S. S. R. K. C. Yamijala, Nonappa and T. Pradeep, *Chem. Mater.*, 2024, **36**, 7581–7594.
77 S. Chandra, A. Sciortino, S. Shandilya, L. Fang, X. Chen, Nonappa, H. Jiang, L. S. Johansson, M. Cannas, J. Ruokolainen, R. H. A. Ras, F. Messina, B. Peng and O. Ikkala, *Adv. Opt. Mater.*, 2023, **11**, 2201901.
78 X. Kang, M. Zhu and A. Han, *Chem. Mater.*, 2019, **31**, 9939–9947.
79 (*a*) R. Jin, C. Zeng, M. Zhou and Y. Chen, *Chem. Rev.*, 2016, **116**, 10346–10413; (*b*) Y. Du, H. Sheng, D. Astruc and M. Zhu, *Chem. Rev.*, 2020, **120**, 526–622; (*c*) X. Kang, Y. Li, M. Zhu and R. Jin, *Chem. Soc. Rev.*, 2020, **49**, 6443–6514; (*d*) J. Yang and R. Jin, *ACS Mater. Lett.*, 2019, **1**, 482–489; (*e*) I. Chakraborty and T. Pradeep, *Chem. Rev.*, 2017, **117**, 8208–8271; (*f*) Nonappa, *Beilstein J. Nanotechnol.*, 2020, **11**, 533–546.
80 (*a*) J. V. Rival, P. Mymoona, K. M. Lakshmi, Nonappa, T. Pradeep and E. S. Shibu, *Small*, 2021, **17**, 2005718; (*b*) V. Linko, H. Zhang, N. Nonappa, M. A. Kostiainen and O. Ikkala, *Acc. Chem. Res.*, 2022, **55**, 1785–1795.
81 (*a*) Nonappa and O. Ikkala, *Adv. Funct. Mater.*, 2018, **28**, 1704328; (*b*) A. Jana, A. R. Kini and T. Pradeep, *AsiaChem Mag.*, 2023, **3**, 56–65; (*c*) A. Nag and T. Pradeep, *ACS Nanosci. Au*, 2022, **2**, 160–178; (*d*) P. Chakraborty, A. Nag, A. Chakraborty and T. Pradeep, *Acc. Chem. Res.*, 2018, **52**, 2–11.
82 (*a*) A. R. Kini, S. Debta, A. Jana, C. Aparna, V. Yadav, N. Kusiak, T. Base, U. V. Waghmare, P. Ghosh and T. Pradeep, *Chem. Mater.*, 2025, **37**, 1284–1296; (*b*) K. S. Sugi, P. Bandyopadhyay, M. Bodiuzzaman, A. Nag, M. Hridya, W. A. Dar, P. Ghosh and T. Pradeep, *Chem. Mater.*, 2020, **32**, 7973–7984.
83 (*a*) N. Alam, A. K. Das, P. Chandrashekar, P. Baidya and S. Mandal, *Nanoscale*, 2024, **16**, 10087–10107; (*b*) P. Chandrashekar, D. A. Varghese, T. Thomas,

A. K. Pal, A. Muraleedharan, A. Salam, M. Ghosh, P. K. Mondal, S. V. Suresh, C. K. Nandi, A. Datta and S. Mandal, *J. Phys. Chem. Lett.*, 2025, **16**, 4107–4113.

84 (*a*) Q.-F. Zhang, P. G. Williard and L.-S. Wang, *Small*, 2016, **12**, 2518–2525; (*b*) M. Bodiuzzaman, W. A. Dar and T. Pradeep, *Small*, 2020, **17**, 2003981.

85 (*a*) L. He, J. Liao, L. Chen, Y. Zhang and Z. Yin, *Angew. Chem., Int. Ed.*, 2019, **58**, 9897–9901; (*b*) W.-Y. Liang, H.-L. Wang, P.-X. Lu, P.-Y. Liao, W. Deng, J.-H. Jia and M.-L. Tong, *Aggregate*, 2025, **6**, e70019.

86 (*a*) S. He, T. Dong, D. Jiang and Q. Zhang, *Coord. Chem. Rev.*, 2025, **539**, 216738; (*b*) L. He, T. Dong, D.-E. Jiang and Q. Zhang, *Coord. Chem. Rev.*, 2025, **535**, 216633.

87 (*a*) A. Chakraborty, H. Dave, B. Mondal, Nonappa, E. Khatun and T. Pradeep, *J. Phys. Chem. B*, 2022, **126**, 1842–1851; (*b*) M. Gharib, A. J. Yates, S. Sanders, J. Gebauer, S. Graf, A. R. Ziefuß, Nonappa, G. Kassier, C. Rehbock, S. Barcikowski, H. Weller, A. Alabastri, P. Nordlander, W. J. Parak and I. Chakraborty, *Adv. Opt. Mater.*, 2024, **12**, 2302833; (*c*) W. Wang, T. Liu, T. Zhao, D. Sun, H. Li, P. Xing and X. Xin, *Adv. Sci.*, 2024, **11**, 2305102; (*d*) K. Sahoo, T. R. Gazi, S. Roy and I. Chakraborty, *Commun. Chem.*, 2023, **6**, 157; (*e*) H. Li, X. Kang and M. Zhu, *Coord. Chem. Rev.*, 2025, **539**, 216738.

88 (*a*) D. Bera, A. Mukhopadhyay, Nonappa and N. Goswami, *J. Phys. Chem. Lett.*, 2023, **14**, 7299–7305; (*b*) D. Bera, S. Mahata, M. Biswas, K. Kumari, S. Rakshit, Nonappa, S. Ghosh and N. Goswami, *Small*, 2025, **21**, 2406551; (*c*) K. S. Sugi, A. P. Sandra, Nonappa, D. Ghosh, J. S. Mohanty, M. P. Kannan, B. S. Sooraj, P. Srikrishnarka, J. Roy, W. A. Darab and T. Pradeep, *Nanoscale*, 2023, **15**, 11927–11934; (*d*) P. Mymoona, J. V. Rival, Nonappa, E. S. S. Shibu and C. Jeyabharathi, *Small*, 2024, **20**, 2308610.

89 G. Schmid, *Chem. Soc. Rev.*, 2008, **37**, 1909–1930.

90 G. Schmid and L. F. Chi, *Adv. Mater.*, 1998, **10**, 515–526.

91 S. Peschel and G. Schmid, *Angew. Chem., Int. Ed. Engl.*, 1995, **34**, 1442–1443.

92 G. Schmid, M. Bäumle and N. Beyer, *Angew. Chem., Int. Ed.*, 2000, **39**, 181–183.

93 N. Ji, Y. Chen, P. Gong and D.-L. Peng, *Colloids Surf., A*, 2015, **480**, 11–18.

94 B. Niesen and B. P. Rand, *Adv. Mater.*, 2014, **26**, 1446–1449.

95 J. V. Rival, S. Chand, A. Jana, Nonappa, V. Biju, T. Pradeep, P. Rajamalli and E. S. Shibu, *Adv. Mater.*, 2025, **37**, e2507893.

96 Z. Qin, Z. Li, S. Sharma, Y. Peng, R. Jin and G. Li, *Research*, 2022, 0018.

97 S. Chandra, A. Sciortino, S. Das, F. Ahmed, A. Jana, J. Roy, D. Li, V. Liljeström, H. Jiang, L.-S. Johansson, X. Chen, M. Cannas, T. Pradeep, B. Peng, R. H. A. Ras, Z. Sun, O. Ikkala and F. Messina, *Adv. Opt. Mater.*, 2023, **11**, 2202649.

98 G. Schmid and N. Beyer, *Eur. J. Inorg. Chem.*, 2000, 835–837.

99 O. Vidoni, T. Reuter, V. Torma, W. Meyer-Zaika and G. Schmid, *J. Mater. Chem.*, 2001, **11**, 3188–3190.

100 S. Liu, R. Maoz, G. Schmid and J. Sagiv, *Nano Lett.*, 2002, **2**, 1055–1060.

101 D. Wyrwa, N. Beyer and G. Schmid, *Nano Lett.*, 2002, **2**, 419–421.

102 T. S. Selvam, C.-M. Chiang and K.-M. Chi, *J. Nanopart. Res.*, 2011, **13**, 3275–3286.

103 Z. Wu, G. Dong, Y. Li, H. Hao, H. Zhang, Z. Lu and B. Yang, *Angew. Chem., Int. Ed.*, 2013, **52**, 9952–9955.

104 Z. Wu, J. Liu, Y. Li, Z. Cheng, T. Li, H. Zhang, Z. Lu and B. Yang, *ACS Nano*, 2015, **9**, 6315–6323.

105 Z. Wu, Q. Yao, S. Zang and J. Xie, *ACS Mater. Lett.*, 2019, **1**, 237–248.

106 Q. Yao, X. Yuan, Y. Yu, Y. Yu, J. Xie, J. Yan and J. Y. Lee, *J. Am. Chem. Soc.*, 2015, **137**, 2128–2135.

107 Y. Hou, Y. Wang, T. Xu, Z. Wang, W. Tian, D. Sun, X. Yu, P. Xing, J. Shen, X. Xin and J. Hao, *Chem. Mater.*, 2022, **34**, 8013–8021.

108 R. Nakatani, S. Biswas, T. Irie, J. Sakai, D. Hirayama, T. Kawawaki, Y. Niihori, S. Das and Y. Negishi, *Nanoscale*, 2023, **15**, 16299.

109 M. Paul, S. Basu and A. Chattopadhyay, *Langmuir*, 2020, **36**, 754–759.

110 W. A. Dar, A. Jana, K. S. Sugi, G. Paramasivam, M. Bodiuzzaman, E. Khatun, A. Som, A. Mahendranath, A. Chakraborty and T. Pradeep, *Chem. Mater.*, 2022, **34**, 4703–4711.

111 Nonappa, T. Lahtinen, J. S. Haataja, T.-R. Tero, H. Häkkinen and O. Ikkala, *Angew. Chem., Int. Ed.*, 2016, **55**, 16035–16038.

112 Nonappa, J. S. Haataja, J. V. I. Timonen, S. Malola, P. Engelhardt, N. Houbenov, M. Lahtinen, H. Häkkinen and O. Ikkala, *Angew. Chem., Int. Ed.*, 2017, **56**, 6473–6477.

113 (*a*) A. Desireddy, B. E. Conn, J. Guo, B. Yoon, R. N. Barnett, B. M. Monahan, K. Kirschbaum, W. P. Griffith, R. L. Whetten, U. Landman and T. P. Bigioni, *Nature*, 2013, **501**, 399; (*b*) B. Yoon, W. D. Luedtke, R. N. Barnett, J. Gao, A. Desireddy, B. E. Conn, T. P. Bigioni and U. Landman, *Nat. Mater.*, 2014, **13**, 807.

114 A. Som, A. Griffo, I. Chakraborty, H. Hähl, B. Mondal, A. Chakraborty, K. Jacobs, P. Laaksonen, O. Ikkala, T. Pradeep and Nonappa, *Small*, 2022, **18**, 2201707.

115 (*a*) A. Som, I. Chakraborty, T. A. Maark, S. Bhat and T. Pradeep, *Adv. Mater.*, 2016, **28**, 2827–2833; (*b*) A. Chakraborty, A. C. Fernandez, A. Som, B. Mondal, G. Natarajan, G. Paramasivam, T. Lahtinen, H. Häkkinen, Nonappa and T. Pradeep, *Angew. Chem., Int. Ed.*, 2018, **57**, 6522–6526.

116 M. Swierczewski, P. Maroni, A. Chenneviere, M. M. Dadras, L.-T. Lee and T. Bürgi, *Small*, 2021, **17**, 2005954.